Dynamic modelling suggests differential mechanisms for initiation of non-selective autophagy and mitophagy

Piero Dalle Pezze, Eleftherios Karanasios, Varvara Kandia, Simon A. Walker, Nicholas T. Ktistakis, and Nicolas Le Novère

The Babraham Institute, Babraham Research Campus, Cambridge, CB22 3AT, UK

Corresponding Author

Nicolas Le Novère, PhD

The Babraham Institute

Babraham Research Campus

Cambridge, CB22 3AT, UK

Telephone: +44-1223-496433

E-mail: nicolas.lenovere@babraham.ac.uk

ORCID: 0000-0002-6309-7327

Keywords

ATG13, autophagy, LC3, mathematical modelling, mitophagy, ULK1

Abbreviations

AIC: Akaike Information Criterion

ATG13: Autophagy-related protein 13

CI: Confidence interval

CL: Confidence level

EC50: Half maximal effective concentration

IVM: Ivermectin drug

LC3: Microtubule-associated proteins 1A/1B light chain 3B

ODE: Ordinary Differential Equation

PI3P: Phosphatidylinositol 3-phosphate

ULK1: Unc-51 like autophagy activating kinase 1

VPS34: Phosphatidylinositol 3-kinase VPS34

Running Title

ATG13 dynamics in non-selective and selective autophagy

Abstract

In the initiation phase of autophagy, the ULK1 complex translocates to endoplasmic reticulum membranes which eventually give rise to autophagosomes via an omegasome intermediate. We studied ULK1 complex accumulation in both starvation-induced non-selective autophagy and ivermectin-induced selective autophagy of mitochondria (mitophagy) using fluorescence imaging and mathematical modelling. In non-selective autophagy, a single accumulation event occurred, whose intensity and duration were reduced upon wortmannin-dependent inhibition of the Class III PI-3 kinase VPS34 and a block in omegasome formation. In contrast, oscillatory dynamics were observed in mitophagy, with increasing time between peaks. We hypothesise that these oscillations reveal successive ULK1 complex translocations, each similar to the event observed in non-selective autophagy. These translocations would only happen on portions of the

mitochondrial surface not already covered by LC3-containing autophagosomal membrane. Our mathematical model reproduced ULK1 repeated aggregations (oscillations) and predicted a positive correlation between the number of events and the mitochondrial diameter.

Introduction

Autophagy is a conserved intracellular pathway that is activated under specific conditions including starvation and low energy levels within the cell, with the purpose of promoting cell survival by recycling cytoplasmic material (Mizushima and Komatsu, 2011; Mizushima et al 2011; Ktistakis and Tooze, 2016). This recycling process involves the formation of a novel double membrane organelle - named the autophagosome - which engulfs and delivers its cargo to the lysosome for degradation (Feng et al 2014; Ohsumi, 2014). Autophagy can be non-selective (or bulk) when the cargo is generic cytoplasmic material, providing the cell with a mechanism of nutrient supply for periods of starvation (Dunlop and Tee, 2014; Mony et al, 2016). Alternatively, autophagy can be selective when it leads to the degradation of specific intracellular structures such as damaged mitochondria, endoplasmic reticulum fragments or bacterial pathogens, forming the basis for a crucial cellular quality control system (Okamoto, 2014; Stolz et al, 2014; Randow and Youle, 2014; Anding and Baehrecke, 2017).

The starvation-induced pathway for the formation of autophagosomes utilises a series of membrane re-arrangements which are formed after a cascade of signals starting with the inactivation of the protein kinase complex mTORC1 (Saxton and Sabatini, 2017). This leads to the activation of the autophagy-specific protein kinase complex ULK formed by the protein kinase ULK1 (or its homologue ULK2), and the adaptors FIP200, ATG13, and ATG101 (Lin and Hurley, 2016; Wong et al, 2013). Once active, the ULK1 complex translocates to

tubulovesicular regions of the ER which are characterised by the presence of vesicles containing the autophagy-specific ATG9 protein. On these sites the lipid kinase VPS34 complex I also translocates to produce PI3P and generate omegasomes (Walker et al, 2008; Karanasios et al, 2016). Karanasios et al, 2013 proposed a PI3P-dependent positive feedback loop occurring in the early phases of omegasome-ULK1 expansion. PI3P binds WIPI proteins, which in turn bind to ATG16 protein, linking the extension of autophagosome membrane to the complexes covalently modifying LC3/GABARAP - the protein binding autophagosome cargo - with phosphatidylethanolamine (Wilson et al, 2014; Yu et al, 2017). In the case of selective autophagy, additional specific proteins are necessary to label the cargo and connect it with the forming autophagosome (Johansen and Lamark, 2011; Rogov et al 2014). Most of these selective autophagy receptors are conserved between yeast and mammals (Khaminets et al, 2016). In yeast, examples include ATG32 for mitochondrial autophagy (mitophagy, Okamoto et al, 2009; Kanki et al, 2009), ATG39/ATG40 for autophagy of ER membranes (Mochida et al, 2015), ATG36/ATG30 for autophagy of peroxisomes (pexophagy, Motley et al, 2012; Nazarko et al, 2014), and ATG19/ATG34 for the Cvt pathway (Scott et al, 2001; Suzuki et al, 2010; Watanabe et al, 2010). The mechanism determining the dynamics and interaction between the selective autophagy receptor proteins and autophagy machinery is currently under investigation, and we have provided some insights in a recent publication (Zachari et al, 2018).

The presence of damage in the mitochondria can trigger mitophagy via the ubiquitination of mitochondrial outer membrane proteins, which are then recognised by mitophagy receptors (Dikic et al, 2017; Kwon and Ciechanover, 2017). A well-studied example of ubiquitin-dependent mitophagy is the pathway regulated by PINK1 and Parkin proteins (Narendra et al, 2008; Nguyen et al, 2016). Alternatively, some mitochondrial proteins can sense certain types of mitochondrial damage, such as a decline in the mitochondrial

membrane potential (Khaminets et al, 2015; Roberts et al, 2016), and act as mitophagy receptors directly. In either case, triggering these mitophagy receptors leads to the recruitment of the LC3/GABARAP proteins, enabling the engulfment of the targeted mitochondrion (Khaminets et al, 2016; Yamano et al, 2016). Certain pharmacological drugs can also induce mitophagy in tissue culture cells (Georgakopoulos et al, 2017), usually affecting the mitochondrial membrane potential or metabolite balance of the mitochondrial lumen. In contrast to these drugs which require several hours to take effect, the anthelmintic lactone ivermectin (IVM) was also found to induce mitochondrial fragmentation within 30 minutes of treatment followed by mitophagy, making it an ideal tool in our study (Zachari et al, 2018).

Data-driven mathematical modelling has been a valuable method for describing biological signalling networks and investigating novel regulatory mechanisms (Kholodenko et al, 2010; Le Novère, 2015; Tomlin and Axelrod, 2007). With respect to autophagy, Martin et al, 2012, designed a computational model using live-cell fluorescent microscopy to characterise autophagic vesicle dynamics in single mammalian cells and to predict the vesicle size. Mathematical models have been proposed for the upstream signalling of autophagosome formation. Szymańska et al, 2015 predicted bistable switching or oscillations between autophagy and protein synthesis within the AMPK-MTORC1- ULK1 network. Dalle Pezze et al, 2016 predicted and showed that amino acid sufficiency can activate AMPK concurrently with mTOR, and activate ULK1 and c-Jun. Mathematical models have also been built for cellular senescence, a state of irreversible cell cycle arrest, which contributes to ageing. Using these models, Dalle Pezze et al, 2014 proposed that impairment of mitochondrial turnover, including via mitophagy, coupled with increased mitochondrial biogenesis provided a mechanism explaining long-term failure in drug intervention to reverse cellular senescence.

In this work, we used complementary *in-vitro* and *in-silico* approaches to investigate the dynamics of the ULK1 complex in the initiation of non-selective autophagy and ivermectin-dependent mitophagy. Using quantitative imaging and mathematical modelling we analysed ULK1 complex translocation for both autophagic modes using fluorescently labelled ATG13 as a surrogate for the complex, something which has been validated several times before (Karanasios et al, 2013; Karanasios et al 2016). We found that whilst non-selective autophagy is characterised by a single event of ULK complex translocation to pre-autophagic puncta, initiating the accumulation of LC3, the process regulating the early steps of mitophagy requires multiple successive such translocations. Our results offer novel insights on the early steps of non- selective and selective autophagy.

Results

A mathematical model for non-selective autophagy

The early steps of autophagosome formation were quantified using wide field imaging data for GFP-ATG13 and CFP-LC3, or GFP-DFCP1 and CFP-LC3 (**Supplementary Figure S1**). ATG13 initiates the process, stimulating PI3P synthesis and omegasome formation followed by the recruitment of PI3P effectors such as DFCP1 (Mizushima and Komatsu, 2011). Following the omegasome formation, LC3-dependent membrane slowly increases as the cargo accumulates. Once mature, the autophagosome detaches from the ER membrane, leading the cargo to the lysosome. Examples of this final event are shown in repeats 3 and 6 for LC3 in Exp2, when the signal dramatically decreases (**Supplementary Figure S1A**) and have been also shown in Karanasios et al 2013. To improve the detection and localisation of fluorescence signals from the developing autophagosome within the cell volume, we decided

to collect z-stacks over time using a spinning disc confocal microscope, focussing on ATG13 as the main readout in our study. Using the spinning disk and collecting all z-stacks encompassing the cell ensures that dynamic structures such as the ATG13-containing puncta will not be lost during the imaging sequence.

To generate a mathematical model of the earliest visible accumulation of autophagic structures in non-selective autophagy, ULK1 complex time course data was collected using fluorescent ATG13 in presence and absence of the PI3K inhibitor wortmannin. Representative time course images for one autophagy event are shown in **Figure 1A**. The presence of wortmannin triggers a reduction of the ATG13 punctum fluorescence intensity and its lifetime, confirming the proposed PI3P-dependent positive regulation of ATG13 signalling (Karanasios et al, 2013). Autophagy events occur in the cytoplasm without synchronisation and the signal at the beginning of the aggregation makes it difficult to determine an exact starting time point. Therefore, we synchronised the time courses data using ATG13 maximum intensity peak (see **Materials and Methods** for details).

We built a minimalistic model for the early steps of non-selective autophagy (**Figure 1B**), where ATG13 aggregates and dissociates following mass action reactions. Due to the noticeable non-linearity of ATG13 accumulation and removal processes, we had to include a dependency for the process on the concentration of aggregated ATG13, with a partial reaction order m. To investigate the effect of wortmannin on these reactions, three models were investigated: 1) wortmannin regulating ATG13 aggregation, 2) wortmannin regulating ATG13 dissociation, and 3) wortmannin regulating both aggregation and dissociation. As ATG13 accumulation time courses were characterised by a rapid increase followed by a steep decrease, we tested two additional hypotheses. In the first, the switch between ATG13 accumulation and removal was regulated by an event happening after t seconds from the

initiation of the process. This delay was estimated from the imaging data. In the second, the reactions of ATG13 accumulation and removal happened simultaneously without any additional regulation. The complete description of the model is given in **Supplementary Tables S1-4**.

Parameter estimation was performed for the six model variants independently and the model fitting against the data is reported in **Figure 1C**. As the number of parameters is different according to the model, we compared their fit quality using the Akaike Information Criterion (AIC) (Akaike, 1974), which penalises models with a higher number of estimated parameters (**Supplementary Table S5**). The only models fitting the data featured wortmannin-regulated ATG13 accumulation and event-triggered dissociation. Due to there being no significant difference between the fitting of either models (Models 1 and 3), we selected the model where wortmannin affects both aggregation and dissociation (Model 3) as the starting point for our study, as it offered a more general biological mechanism. This model was also the only one where all the parameters were identifiable with a 66% confidence level (**Supplementary Table S3**). Surprisingly, parameter estimation revealed a value of 1.01365 for the parameter *m* (confidence interval at 66%: [0.164715, 1.60609]) representing the partial reaction order of ULK1 complex accumulation on the already aggregated complex. This suggests significant cooperativity for ULK1 complex accumulation. Details for parameter estimation and identifiability are reported in the **Materials and Methods**, **Supplementary Table S3 and Supplementary Figure S1**.

Wortmannin affects ATG13 peak time distribution in non-selective autophagy

Since a PI3P feedback on the initiation of autophagosome formation had been suggested, we analysed the effect of wortmannin on a population of non-selective autophagy events (puncta) using ATG13 as a readout. This was done by analysing the ATG13 peak times

upon starvation (**Figure 2A**) and starvation plus wortmannin (**Figure 2B**). First we verified that there was no significant correlation between the signal peak times and initial signal intensities, which could have pointed to a possible misidentification of the start of aggregation and therefore of signal peak times (**Supplementary Figure S3**).The signal intensity of each experimental time course repeat was then normalised within [0,1]. Sorting repeats by decreasing peak times (dark red points in Figure A and B) suggests that addition of wortmannin changes their probability distribution, whereas without wortmannin it follows a more sigmoid shape. Q-Q plots for ATG13 peak times upon starvation (**Figure 2C**) and starvation plus wortmannin (**Figure 2D**) versus normal or log-normal distributions suggested that the peak times for ATG13 fluorescence signal upon starvation tended to approximate a normal distribution, whereas wortmannin shifted the peak times to approximate a log-normal distribution. This result was more clearly highlighted by the overlapping of the data set densities and the corresponding theoretical normal and log-normal probability densities computed with parameters from **Supplementary Table S6**. We statistically tested whether the peak times were normally distributed. The Shapiro-Wilk test could not reject the null-hypothesis that the starvation without wortmannin group was normally distributed (*p*-value: 0.432; skewness: 0.312, excess kurtosis: -0.251), but did reject the null-hypothesis for the starvation plus wortmannin group (*p*-value: 0.004; skewness: 1.193, excess kurtosis: 1.716). If the data are log-normally distributed the logarithms of the data are expected to be normal. The Shapiro-Wilk test using the logarithms of the starvation plus wortmannin group could not reject the null-hypothesis (*p*-value: 0.855), suggesting that this data set could be normally distributed. The skewness and excess kurtosis for this set were very close to 0 (skewness: -0.116, excess kurtosis: -0.198), indicating that the distribution is almost normal and supporting the original thesis that the starvation plus wortmannin group is log-normally distributed. Using model 3 described above, we can simulate populations of non-selective autophagy events with and without wortmannin, where the peak time (parameter *t*) was

sampled from a normal or log-normal distribution respectively (parameters for both normal and log-normal distribution are reported in **Supplementary Table S6**). Those simulations adequately reproduce the experimental data, and suggest that our model can be used to describe the initial step of autophagosome formation.

A mathematical model for mitophagy

In contrast to the non-selective autophagy data set which was generated upon starvation conditions, the drug Ivermectin was used for triggering mitophagy events (see Zachari et al, 2018). A total of 23 fluorescence imaging time courses for ATG13 were retained after checking that the protein co-localised with the targeted mitochondrion for the whole duration of the time course and formed a quasi-ring structure around the mitochondrion at some point along the time course. This excluded events of non-selective autophagosome formation on the mitochondria surface.

Representative time course images are shown in **Figure 3A**. In contrast to the non-selective autophagy, where there was a single peak of ATG13, in mitophagy ATG13 appeared to join and leave the targeted mitochondrion several times, triggering oscillatory dynamics. Time courses were quantified, synchronised, filtered and regularised (see **Materials and Methods** for details). **Figure 3B** shows three examples of time courses and **Figure 3C** shows the final mean time course from the 17 datasets including confidence interval of the mean at 95% confidence level and 1 standard deviation. From the mean time course we identified the peaks and troughs for each aggregation event. We show that the delay between events tends to increase exponentially along the time course (**Figure 3D**).

Like non-selective autophagy, the ULK1 complex initiates a cascading mechanism that leads to mitochondrion engulfment by the LC3-covered membrane. To explain the observed repeated peaks of ATG13, separated by increasing delays, we made the hypothesis that

ULK1 complexes can only aggregate in regions of the mitochondrion surface not already covered by LC3 containing membrane. As the engulfment progresses, the portion of mitochondrial surface not covered by LC3 decreases, and the probability of a new translocation event decreases. This process continues until the whole mitochondrion has been engulfed by LC3 containing membrane. We extended the model developed for non-selective autophagy in order to include LC3 (**Figure 3E**). LC3 accumulation is driven by the presence of ATG13-containing complexes (see also Karanasios et al, 2013), and it in turn feeds back on those complexes by decreasing the probability of initiating a new aggregation event. The complete description of the model is given in **Supplementary Tables S7-10**.

We fitted the model with the mitophagy time course data. First, in order to parametrise ULK1 complex aggregation and dissociation, we extracted the first peak of each time course and synchronised them as we did for the non-selective autophagy data set (**Figure 3F**, **Supplementary Table S9**, and **Supplementary Figure S4.** See **Materials and Methods** for details). Parameter estimation revealed that the ATG13 kinetic rate constants were not significantly different between the mitophagy model (parameters: kprodATG13 = 0.0114, CI95 = [0.0099, 0.0127]; kremATG13 = 0.0114, CI95 = [0.0010, 0.0139]) and the non-selective autophagy model (parameters: kprodATG13 = 0.0082, CI95=[0.0052, 0.0193]; kremATG13 = 0.0029, CI95=[0.0007, 0.0183]). Second, we estimated the remaining model parameters using the complete ATG13 time course data set. In the model there are two parameters sampled from random variables. The first one is the time between the start of an aggregation event and the peak of ATG13 concentration, which is sampled at each aggregation (parameter *t* as in the non-selective autophagy model). As the ATG13 peak times upon starvation in the non-selective autophagy were largely normally distributed (**Figure 2C**), we assumed that this was still the case during mitophagy. We directly extracted

the information needed to compute *t* from the time differences between upper and lower peaks in **Figure 3D**. Detailed statistics are reported in **Supplementary Table S11**. The second parameter is the mitochondrial diameter which is randomly sampled at the beginning of each time course from the distribution of measured mitochondrial diameters. By analysing the mitochondrial diameters from the imaging time courses, we found that the population approximated a normal distribution (**Figure 3G**, **Supplementary Figure S5**). In agreement with this observation, Shapiro-Wilk statistical test could not reject the null hypothesis that these data were normally distributed (*p*-value: 0.379; skewness: 0.378, excess kurtosis: -1.061). In order to fit the mean experimental time course (**Figure 3C**) we fixed the values of time to peak and mitochondrial diameter to the mean of their experimental distributions as reported in **Figures 3D, 3G (second plot)**. **Figure 3H** shows the fitting between model and data. Details for parameter estimation and identifiability are reported in the **Materials and Methods**. Parameter estimation gave an insight about the increasing delay between aggregations. In particular, the parameter *p* determining the exponential increase for the delay was estimated to be ~2.79. At first, this high value was a surprise as we were expecting that the delay between aggregations grew quadratically with time, in proportion with the surface coverage by LC3. However, as in our hypothesis each aggregation event represents a local coverage by both ATG13 and LC3, a cubic growth could be explained by the combination of the time ATG13 requires to search for the next available region to cover and the time for the LC3 modifying machinery to translocate onto the current placement of ATG13.

MT diameter determines the number of ULK1-complex aggregation events

According to our hypothesis, each occurrence of ULK1-complex aggregation promotes a partial coverage of a mitochondrion by LC3-containing membrane, and this process terminates when the whole mitochondrion becomes engulfed (see **Figure 4A**). Therefore,

the increasing delay between observed ATG13 peaks is due to two phenomena: 1) the time spent by the ULK1 complex searching a region on the mitochondrion surface which has not yet been covered by LC3 membrane, and 2) the translocation of the LC3-modifying machinery. Under the assumption that the ULK1 complex drives engulfment by LC3, the latter delay should be constant over time as no random search is involved. Therefore, our model explicitly represents only the ULK1-dependent delay.

Using the parameters estimated above, we simulated 17 mitophagy events. In order to simulate mitochondria of different sizes, the parameter *MT_diam* - determining the mitochondria diameter within the model - was sampled from a normal distribution inferred from the data at the beginning of each simulation (see distribution parameters in **Figure 3G plot 2, Supplementary Table S10**). The parameter *t*, setting the time between the beginning and the maximum signal of each ATG13 aggregation event, was also sampled from a normal distribution inferred from the data at the beginning of each ATG13 accumulation (see distribution parameters in **Figure 3D, Supplementary Tables S10-11**). The single simulation repeats for the main model readouts are shown in **Figure 4B**. The oscillations for a population of mitophagy events tend to lose synchronisation over time due to the stochastic increase in delay between peaks. The normal distribution of aggregation duration means that the quantity of LC3-membrane for each aggregation event of ULK1 complex will also be normal. This suggested that the size of a mitochondrion could determine the total number of accumulations needed to fully engulf it. Therefore, we analysed whether there was a correlation between the number of ATG13 peaks and the sampled mitochondrial diameters. This analysis was conducted at the end of the simulation (910 s), and in the middle (500 s). Indeed, the simulated data predicted a significant linear positive correlation ($r = 0.88$, p-value = 3.3e-0.6) between the number of ATG13 aggregations and the diameters of the corresponding engulfed mitochondria at the end of

the simulation (**Figure 4C**). To test this prediction, we counted the number of peaks for the 17 repeats in our experimental data and plotted them against the corresponding mitochondrial diameters, revealing a significant linear positive correlation (r = 0.87, *p*-value = 4.3e-06) (**Figure 4D**).

Inhibition of PI3P or LC3 feedbacks should impact ULK1-complex dynamics

Having proposed a mechanism for a progressive mitochondrial engulfment by LC3-containing membranes, we were interested to evaluate the impact of the two feedback loops present in the model. To do so, we simulated two perturbations of the model and compared them against the control prediction results shown as separate repeats in **Figure 4B** and summarised time courses in **Figure 5A**.

In the first intervention, we assessed the VPS34 positive feedback loop on ULK1-complex accumulation by simulating the effect of wortmannin inhibition using the same inhibition coefficient (parameter *kwrtm*) estimated for the non-selective autophagy model. As in the non-selective autophagy data, we made the hypothesis that the duration of ULK1-complex accumulation (parameter *t*) was log-normally distributed, and the parameter *t* was thus sampled from a log-normal distribution using the distribution parameters in **Supplementary Table S11**. The mitochondrial diameters were sampled from the same normal distribution as in the control model. This treatment caused an increase in the number of peaks and an overall reduction in peak amplitude compared to the control (**Figure 5B**). LC3 and the delay between peaks were not significantly affected since the small duration of ATG13 peaks was compensated by an increase in their number. Individual simulations are shown in **Supplementary Figure S6**.

In the second intervention, we simulated the inhibition of LC3 lipidation. To achieve this we simply doubled the *EC50* of ULK1-complex for the production of LC3-containing membrane.

Both the duration of ULK1-complex accumulation and mitochondrial diameters were sampled as in control. The simulations predicted more synchronised repetitions compared to the control prediction (**Figure 5C**). This was due to the fact that less mitochondrial surface was covered by LC3-containing membrane, therefore limiting the increase in stochastic delay between ATG13 peaks. The number of peaks remained fairly constant over time instead of decreasing as in the control prediction. The single repeats for this prediction are shown in **Supplementary Figure S7**.

Discussion

In recent years, we and others have described the early membrane re-arrangements involved in the initiation of autophagy in some detail (Ktistakis and Tooze, 2016). It is very clear from that work that the process is extremely complicated, it involves a series of hierarchical translocations of the relevant components on and off the forming autophagosomes, and it concerns a large number of proteins and protein complexes. Here, we observed one of the earliest events of this pathway, the translocation of the ULK complex to the forming autophagosomal structure, and used mathematical models to gain insight into the mechanisms that regulate it.

Omegasome formation in non-selective autophagy is characterised by a single event of ULK1 complex accumulation. In our model, the cooperative aggregation of ULK1 complex is represented by the model parameter *m*, increasing the partial order of the ATG13 species for the reactions of accumulation and removal. Model parameter estimation partially identified this parameter and calculated a positive value, supporting the hypothesis of a positive feedback loop increasing and decreasing the rate of ATG13 accumulation and removal, respectively. Such a cooperativity could be explained for instance by a surface effect. The larger the ULK1 complex aggregates, the more sites there are for aggregation or

disassembly. Moreover, Karanasios et al, 2013 speculated that a PI3P-dependent positive feedback loop is responsible for the concomitant expansion of the ULK1 complex and omegasome in the early steps of non-selective autophagy. Upon wortmannin-dependent inhibition of the VPS34 Complex, which regulates PI3P production, the VPS34-ULK1 positive feedback loop was altered. This led to a decrease in duration and intensity of ATG13 aggregations and a change in the probability distribution of ATG13 peak times from normal to log-normal. One possible explanation is that wortmannin-dependent PI3P inhibition removes external controls on ULK1 complex accumulation, letting the process be only driven by complex stability. Without external factors, many natural phenomena relating to frequencies, e.g. in this case the kinetics of ULK1-based structure disaggregation (**Figure 2D**), can be described and explained by a log-normal distribution (Hosoda et al, 2011; Limpert et al, 2001). As the noise of upstream PI3P signalling pathways is normally distributed due to the many steps involved, the native log-normal distribution of the times of ULK1-based structure disaggregation becomes masked by a normal distribution (**Figure 2C**).

In contrast to non-selective autophagy, in mitophagy ULK1 complex accumulation and removal are orchestrated via a sequence of events. According to our hypothesis, in each of these events ULK1 complex aggregate on LC3-free subsurface on the targeted mitochondrion and drives the subsequent coverage by LC3 membrane of this region. Using time-course data analysis and mathematical modelling, we showed that these events delay exponentially along the time course. In addition, model simulations predicted, and experimental data confirmed, that their number are proportional to the mitochondrial diameter. These findings indicate that mitophagy is dependent on the target structure and that the ULK1/2 complex is a key component for this process. How does ULK1/2 complex locate an LC3-free subsurface on the mitochondrion? A potential explanation could be that

ULK1/2 can only accumulate on a region on the mitochondrion where mitophagy receptors can be detected. Therefore, a region partially engulfed by LC3 would prevent the binding between ULK1/2 and these mitophagy receptors.

Our study also analysed the delay between ATG13 events. Model parameter estimation reveals that the delay between ATG13 events on the targeted mitochondrion increases almost cubically along the time course. Because the ULK1 complex covers a surface, the delay between each step of partial engulfment is expected to grow quadratically. As the number of ATG13 events inherently depends on LC3 partial engulfment of the targeted mitochondrion, it appears clear that the translocation and engulfment of the LC3 machinery onto the mitochondrion surface adds an additional delay, and that our model calibration estimates the sum of the ATG13- and LC3-dependent delays. A future model based on ATG13 and LC3 data could better separate the respective contributions to the overall delay.

Materials and Methods

Cell cultures

HEK-293 cells stably expressing GFP-ATG13 have been described before (Karanasios et al, 2013). Immunofluorescence microscopy was performed as described in Karanasios et al, 2015. Mitophagy experiments were performed as described in Karanasios et al, 2016, and Zachari et al, 2018.

Raw data acquisition

Images were acquired using a spinning disk confocal microscope, comprising Nikon Ti-E stand, Nikon 100x 1.49 NA objective, Yokogawa CSU-X scanhead, Andor TuCam splitter

and Andor iXon 897 EM-CCD cameras. Using the splitter and 2x cameras enabled GFP (ATG13) and mCherry (mitochondria) images to be captured simultaneously. Images comprising 512x512 160 nm pixels were taken using a 200-300 ms exposure time, with z-stacks acquired at 10 s intervals. Each stack covered ~6 µm range, with the step interval set at 500-700 nm to ensure optimal sampling. Maximum intensity projections of cropped regions were created using FIJI (Schindelin et al, 2012) and analysed using Imaris software v9.1.2 (http://www.bitplane.com) to quantify mean signal intensities along the time course. To generate the non-selective autophagy data set, raw confocal images were acquired from 8 cells. From these images, 37 non-selective autophagy events were selected upon starvation and 40 events upon starvation plus wortmannin, measuring ATG13 as readout. As autophagy events were triggered within the cytoplasm at different time points, we synchronised the time courses based on their maximum intensity peak. To generate the mitophagy data set, raw confocal images were acquired from 25 cells and 23 events were selected assuring that ATG13 (green channel) co-localised with a mitochondrion (red channel) and ATG13 formed a quasi-circle around the mitochondrion at some point within the time course. This allowed us to exclude potential autophagosome formation on the mitochondrion surface. This selection of mitophagy events was then quantified (**Supplementary Figure S8**). Then, the time courses were manually synchronised, overlapping the delays between aggregations. To facilitate the synchronisation, the time courses were splined reducing the noise within the data (**Supplementary Figure S9**). Once synchronised, the splined time courses were replaced with the original time courses (**Supplementary Figure S10**, **AB**). Six time courses were removed due to their highly irregular nature. The initial and late time points were also cut off in order to have at least three repeats for each time point (**Supplementary Figure S10**, **C**). Finally, the time courses were regularised to eliminate the gradual signal decline typically occurring over time in

fluorescence images (**Supplementary Figure S10**, **D**). The final single regularised time courses are reported in **Supplementary Figure S11**.

Mitochondria diameters were extracted using ImageJ 1.51 (Schneider et al, 2012). At least 8 mitochondria diameter measurements were taken for each of the 17 time courses (**Supplementary Figure S5**). The averages of these measurements were then computed and summarised in **Figure 3G**.

ATG13 model in non-selective autophagy

Parameter estimation was performed using Copasi 4.22 (Hoops et al, 2006) and SBpipe 4.20.0 (Dalle Pezze and Le Novère, 2017). Particle Swarm optimisation algorithm as implemented in Copasi was configured as follows: iteration number=1000, and swarm size=100. SBpipe was configured to run 1000 parameter estimates using Copasi within the SGE cluster at the Babraham Institute (UK).

The mathematical description for the non-selective autophagy model including its events and parameters is reported in **Supplementary Tables S1-4**. Synchronised time courses for ATG13 upon starvation and starvation plus wortmannin were simultaneously used as data sets for parameter estimation. The parameters (*kprodATG13*, *kremATG13*, *m*, *kwrtm*, *t*) were estimated for the models 1-3. The same parameters except *t* were estimated for models 4-6, as these models do not include events. For each of the six model variants, a total of 1000 parameter estimates were independently calculated. The 75% of the best fits (reporting the lowest objective value) were selected for analysis. Profile Likelihood Estimation (PLE) analysis was executed at the confidence levels of 66%, 95%, and 99% (**Supplementary Table S3**, **Supplementary Figure S1**). Due to the different number of estimated parameters, the AIC was used for ranking the model variants (**Supplementary Table S5**).

ATG13 mitophagy model

The mitophagy model extended the non-selective autophagy model with the inclusion of LC3 and oscillatory dynamics with delay for ATG13. The mathematical description for the mitophagy model including its events and parameters is reported in **Supplementary Tables S7-10**. Parameter estimation for the mitophagy model was performed in two steps. Firstly, the first aggregation of ATG13 time courses was extracted and synchronised on the peak of maximum signal intensity as for the non-selective autophagy data. This reduced data set was used for estimating the kinetic rate constants for ATG13 (*kprod_ATG13* and *krem_ATG13*), and therefore compute the slopes of ATG13 signalling independently of the complex oscillatory oscillatory behaviour (**Supplementary Table S9**, **Supplementary Figure S4A**). Secondly, the parameters regulating the repeated aggregations (*kprodLC3*, *kpeak*, *p*) were estimated in two rounds of parameter estimation and identifiability. The first round revealed that *p* and *kprodLC3* were identifiable, although *kprodLC3* minima lay on a defined plateau. Fixing *kprodLC3*, the interdependent parameter *kpeak* was estimated and identified in a second round of parameter estimation (**Supplementary Table S9**, **Supplementary Figure S4BC**). The parameters *t* and *MT_diam*, representing the time before reaching an aggregation peak and the mitochondria diameter respectively, were fixed to the mean of their normal distribution during the second stage of parameter estimation.

Statistics

The statistical and programming language R version 3.4.0 was used to generate statistics and plots. AIC (Akaike, 1974) as computed in SBpipe was used for selecting the non-selective autophagy model which fitted the non-selective autophagy dataset. Shapiro-Wilk test was used for testing normality distribution. A batch correction using R package SVA (Leek et al, 2012) was applied to the intensities of LC3 in **Figure 1A** to make the repeats of the two experiments of comparable intensity levels.

Acknowledgements

We thank our colleagues Len Stephens and Phill Hawkins at the Babraham Institute for many useful discussions. We thank Maria Manifava for preparing all cells for the mitophagy experiments.

Author Contributions

The project was designed by NLN and NTK. Mathematical modelling was performed by PDP. Live imaging data were collected by EK and SAW. Images were analyzed by PDP and VK. The manuscript was written by PDP and NLN with contributions from NTK and SAW.

Funding

This work was funded by the Biotechnology and Biological Sciences Research Council (grant numbers: BBS/E/B/000C0419 and BBS/E/B/000C0434 to NLN; BB/K019155/1 to NTK); and a science policy committee from the Babraham Institute, Cambridge (grant number 2301-R1600-C0341 to NTK).

Conflict of Interest

The authors declare no conflict of interest.

References

1. Mizushima, N. and M. Komatsu. 2011. Autophagy: renovation of cells and tissues. Cell 147:728-41.
2. Mizushima N., T. Yoshimori, and Y. Ohsumi. 2011. The role of Atg proteins in autophagosome formation. Annu Rev Cell Dev Biol. 27:107-32.
3. Ktistakis, N.T., and S.A. Tooze. 2016. Digesting the Expanding Mechanisms of Autophagy. Trends Cell Biol. 26:624-35.
4. Feng, Y., He, D., Yao, Z., and D.J. Klionsky. 2014. The machinery of macroautophagy. Cell Res. 24:24-41.
5. Ohsumi, Y. 2014. Historical landmarks of autophagy research. Cell Res. 24:9-23.
6. Dunlop E.A., and A.R. Tee. 2014. mTOR and autophagy: a dynamic relationship governed by nutrients and energy. Semin Cell Dev Biol. 36:121-9.
7. Mony, V.K., Benjamin, S., and E.J. O'Rourke. 2016. A lysosome-centered view of nutrient homeostasis. Autophagy. 12:619-31.
8. Okamoto, K. 2014. Organellophagy: eliminating cellular building blocks via selective autophagy. J Cell Biol. 205:435-45.
9. Stolz, A., Ernst, A., and I. Dikic. 2014. Cargo recognition and trafficking in selective autophagy. Nat Cell Biol. 16:495-501
10. Randow, F., and R.J Youle. 2014. Self and nonself: how autophagy targets mitochondria and bacteria. Cell Host Microbe. 15:403-11.
11. Anding, A.L., and E.H. Baehrecke. 2017. Cleaning House: Selective Autophagy of Organelles. Dev Cell. 41:10-22.
12. Saxton, R.A., and D.M. Sabatini. 2017. mTOR Signaling in Growth, Metabolism, and Disease. Cell 168:960-976.

13. Lin, M.G., and J.H. Hurley. 2016. Structure and function of the ULK1 complex in autophagy. Curr Opin Cell Biol. 39:61-8.
14. Wong, P.M., Puente, C., Ganley, I.G., and X. Jiang. 2013. The ULK1 complex: sensing nutrient signals for autophagy activation. Autophagy 9:124-37.
15. Walker, S., Chandra, P., Manifava, M., Axe, E., and N.T. Ktistakis. 2008. Making autophagosomes: localized synthesis of phosphatidylinositol 3-phosphate holds the clue. Autophagy 4:1093-6.
16. Karanasios, E., Walker, S.A., Okkenhaug, H., Manifava, M., Hummel, E., Zimmermann, H., Ahmed, Q., Domart, M.C., Collinson, L., and N.T. Ktistakis. 2016. Autophagy initiation by ULK complex assembly on ER tubulovesicular regions marked by ATG9 vesicles. Nat Commun. 7:12420.
17. Karanasios, E., Stapleton, E., Manifava, M., Kaizuka, T., Mizushima, N., Walker, S.A., and N.T. Ktistakis. 2013. Dynamic association of the ULK1 complex with omegasomes during autophagy induction. J Cell Sci. 126:5224-38.
18. Wilson, M.I., Dooley, H.C., and S.A. Tooze. 2014. WIPI2b and Atg16L1: setting the stage for autophagosome formation. Biochem Soc Trans. 42:1327-34.
19. Yu, L., Chen, Y., and S.A. Tooze. 2017. Autophagy pathway: cellular and molecular mechanisms. Autophagy. 14(2):207-215.
20. Johansen, T., and T. Lamark. 2011. Selective autophagy mediated by autophagic adapter proteins. Autophagy 7:279-96.
21. Rogov, V., Dötsch, V., Johansen, T., and V. Kirkin. 2014. Interactions between autophagy receptors and ubiquitin-like proteins form the molecular basis for selective autophagy. Mol Cell. 53:167-78.
22. Khaminets, A., Behl, C., and I. Dikic. 2016. Ubiquitin-Dependent And Independent Signals In Selective Autophagy. Trends Cell Biol. 26:6-16.

23. Okamoto, K., Kondo-Okamoto, N., and Y. Ohsumi. 2009. Mitochondria-anchored receptor Atg32 mediates degradation of mitochondria via selective autophagy. Dev Cell. 17:87-97.

24. Kanki, T., Wang, K., Cao, Y., Baba, M., and D.J. Klionsky. 2009. Atg32 is a mitochondrial protein that confers selectivity during mitophagy. Dev Cell. 17:98-109.

25. Mochida, K., Oikawa, Y., Kimura, Y., Kirisako, H., Hirano, H., Ohsumi, Y., and H. Nakatogawa. 2015. Receptor-mediated selective autophagy degrades the endoplasmic reticulum and the nucleus. Nature. 522:359-62.

26. Motley, A.M., Nuttall, J.M., and E.H. Hettema. 2012. Pex3-anchored Atg36 tags peroxisomes for degradation in Saccharomyces cerevisiae. EMBO J. 31:2852-68.

27. Nazarko, T.Y., Ozeki, K., Till, A., Ramakrishnan, G., Lotfi, P., Yan, M., and S. Subramani. 2014. Peroxisomal Atg37 binds Atg30 or palmitoyl-CoA to regulate phagophore formation during pexophagy. J Cell Biol. 204:541-57.

28. Scott, S.V., Guan, J., Hutchins, M.U., Kim, J., Klionsky, D.J. 2001. Cvt19 is a receptor for the cytoplasm-to-vacuole targeting pathway. Mol Cell:1131-41.

29. Suzuki, K., Kondo, C., Morimoto, M., and Y. Ohsumi. 2010. Selective transport of alpha-mannosidase by autophagic pathways: identification of a novel receptor, Atg34p. J Biol Chem. 285:30019-25

30. Watanabe, Y., Noda, N.N., Kumeta, H., Suzuki, K., Ohsumi, Y., and F. Inagaki F. 2010. Selective transport of alpha-mannosidase by autophagic pathways: structural basis for cargo recognition by Atg19 and Atg34. J Biol Chem. 285:30026-33.

31. Zachari, M., Gudmundsson, S.R., Li, Z., Manifava, M., Shah, R., Smith, M., Stronge, J., Karanasios, E., Kishi-Itakura, C., Vihinen, H., Jokitalo, E., Guan, J., Buss, F., Smith, A.M., Walker, S., Eskelinen, E., Ktistakis, N.T. 2018. Selective autophagy of mitochondria on a ubiquitin-endoplasmic reticulum platform. Submitted.

32. Dikic I. 2017. Proteasomal and Autophagic Degradation Systems. Annu Rev Biochem. 86:193-224.

33. Kwon, Y.T., and A. Ciechanover. 2017. The Ubiquitin Code in the Ubiquitin-Proteasome System and Autophagy. Trends Biochem Sci. 42:873-886.

34. Narendra, D., Tanaka, A., Suen, D.F., and R.J. Youle. 2008. Parkin is recruited selectively to impaired mitochondria and promotes their autophagy. J Cell Biol. 183:795-803.

35. Nguyen, T.N., Padman, B.S., and M. Lazarou. 2016. Deciphering the Molecular Signals of PINK1/Parkin Mitophagy. Trends Cell Biol. 26:733-44.

36. Khaminets, A., Heinrich, T., Mari, M., Grumati, P., Huebner, A.K., Akutsu, M., Liebmann, L., Stolz, A., Nietzsche, S., Koch, N., Mauthe, M., Katona, I., Qualmann, B., Weis, J., Reggiori, F., Kurth, I., Hübner, C.A., and I. Dikic. 2015. Regulation of endoplasmic reticulum turnover by selective autophagy. Nature. 522:354-8.

37. Roberts, R.F., Tang, M.Y., Fon, E.A., and T.M. Durcan. 2016. Defending the mitochondria: The pathways of mitophagy and mitochondrial-derived vesicles. Int J Biochem Cell Biol.79:427-436.

38. Yamano, K., Matsuda, N., and K. Tanaka. 2016. The ubiquitin signal and autophagy: an orchestrated dance leading to mitochondrial degradation. EMBO Rep. 17:300-16.

39. Georgakopoulos, N.D., Wells, G., and M. Campanella. 2017. The pharmacological regulation of cellular mitophagy. Nat Chem Biol. 13:136-146.

40. Kholodenko, B.N., Hancock, J.F., Kolch, W. 2010. Signalling ballet in space and time. Nature Reviews Molecular Cell Biology. 11:414-426.

41. Le Novère, N. 2015. Quantitative and logic modelling of molecular and gene networks. Nature Reviews Genetics. 16:146-158.

42. Tomlin, C.J., Axelrod, J.D. 2007. Biology by numbers: mathematical modelling in developmental biology. Nature Reviews Genetics. 8:331-340.

43. Martin, K.R., Barua, D., Kauffman, A.L., Westrate, L.M., Posner, R.G., Hlavacek, W.S., MacKeigan, J.P. 2012. Computational model for autophagic vesicle dynamics in single cells. Autophagy. 9(1):74-92.

44. Szymańska, P., Martin, K.R., MacKeigan, J.P., Hlavacek, W.S., Lipniacki, T. 2015. Computational Analysis of an Autophagy/Translation Switch Based on Mutual Inhibition of MTORC1 and ULK1. PLoS ONE. 10(3): e0116550.

45. Dalle Pezze, P., Ruf, S., Sonntag, A.G., Langelaar-Makkinje, M., Hall, P., Heberle, A.M., Razquin Navas, P., van Eunen, K., Tölle, R.C., Schwarz, J.J., Wiese, H., Warscheid, B., Deitersen, J., Stork, B., Fäßler, E., Schäuble, S., Hahn, U., Horvatovich, P., Shanley, D.P., Thedieck, K. 2016. A systems study reveals concurrent activation of AMPK and mTOR by amino acids. Nature Communications. 7:13254.

46. Dalle Pezze, P., Nelson, G., Otten, E.G., Korolchuk, V.I., Kirkwood, T.B.L., von Zglinicki, T., and D.P. Shanley. 2014. Dynamic Modelling of Pathways to Cellular Senescence Reveals Strategies for Targeted Interventions. PLoS Comput Biol 10(8):e1003728.

47. Akaike, H. 1974. A new look at the statistical model identification. IEEE Transactions on Automatic Control. 19 (6): 716-723.

48. Hosoda, K., Matsuura, T., Suzuki, H., and T. Yomo. 2011. Origin of lognormal-like distributions with a common width in a growth and division process. Phys Rev E Stat Nonlin Soft Matter Phys. 83(3):031118.

49. Limpert, E., Stahel, W.A., M. Abbt. 2001. Log-normal Distributions across the Sciences: : Keys and Clues. BioScience. 51(5):341-352.

50. Karanasios, E., and N.T. Ktistakis. 2015. Live-cell imaging for the assessment of the dynamics of autophagosome formation: focus on early steps. Methods 75:54-60.

51. Schindelin, J., Arganda-Carreras, I., Frise, E., Kaynig, V., Longair, M., Pietzsch, T., Preibisch, S., Rueden, C., Saalfeld, S., Schmid, B., Tinevez, J., White, D.J., Hartenstein, V., Eliceiri, K., Tomancak, P., and A. Cardona. 2012. Fiji: an open-source platform for biological-image analysis. Nature Methods 9:676-682.

52. Schneider, C.A., Rasband, W.S., and K.W. Eliceiri. 2012. NIH Image to ImageJ: 25 years of image analysis. Nature methods 9(7): 671-675.

53. Hoops, S., Sahle, S., Gauges, R., Lee, C., Pahle, J., Simus, N., Singhal, M., Xu, L., Mendes, P., and U. Kummer. 2006. COPASI - a COmplex PAthway SImulator. Bioinformatics. 22(24):3067-74.

54. Dalle Pezze, P., and N. Le Novère. 2017. SBpipe: a collection of pipelines for automating repetitive simulation and analysis tasks. BMC Syst. Biol. 11:1-1.

55. Leek, J.T., Johnson, W.E., Parker, H.S., Jaffe, A.E., and Storey, J.D. 2012. The sva package for removing batch effects and other unwanted variation in high-throughput experiments. Bioinformatics. 28(6):882-3.

Figure Legends

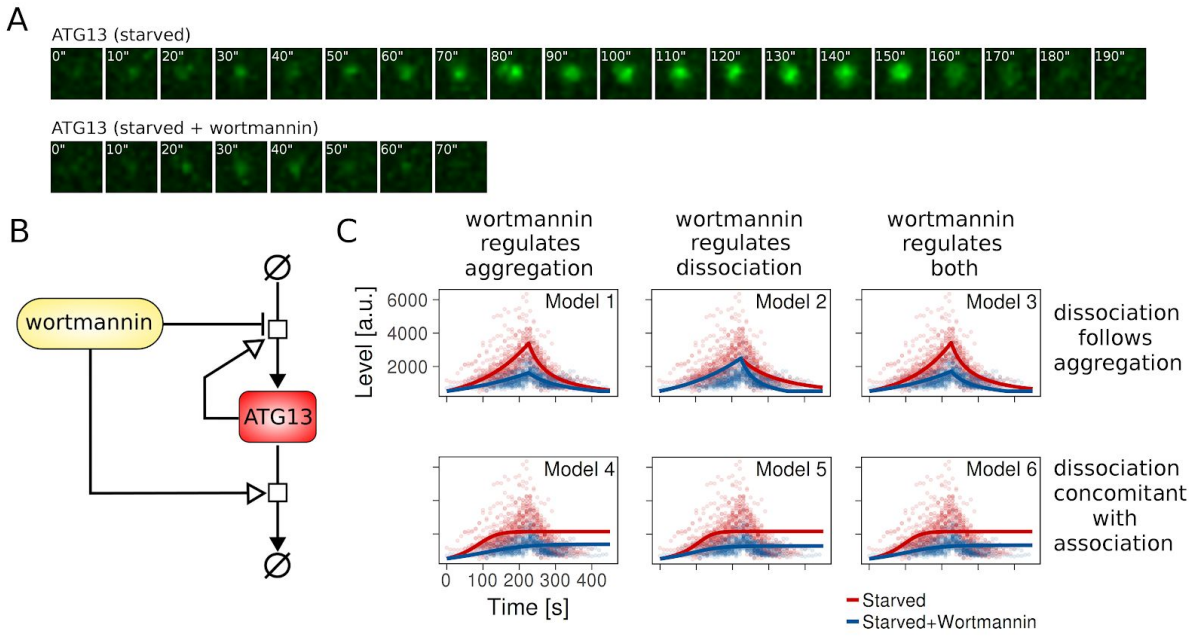

Figure 1. A mathematical model for non-selective autophagy.

A. Representative time course images of one autophagy event. In the first row, cells are starved. In the second row, cells are starved and treated with wortmannin. White arrows indicate ATG13 accumulation.

B. Schematic diagram of the mathematical model for non-selective autophagy.

C. Parameter fitting for the 6 model variants. The switch between ATG13 accumulation and removal is regulated by events in Models 1-3. Models 4-6 are eventless. Wortmannin downregulates ATG13 accumulation (Models 1 and 4), ATG13 removal (Models 2 and 5), and both the reactions (Models 3 and 6). Dots are experimental time points, whereas lines indicate model simulation after parameter estimation. Red indicates starvation, blue indicate starvation plus wortmannin.

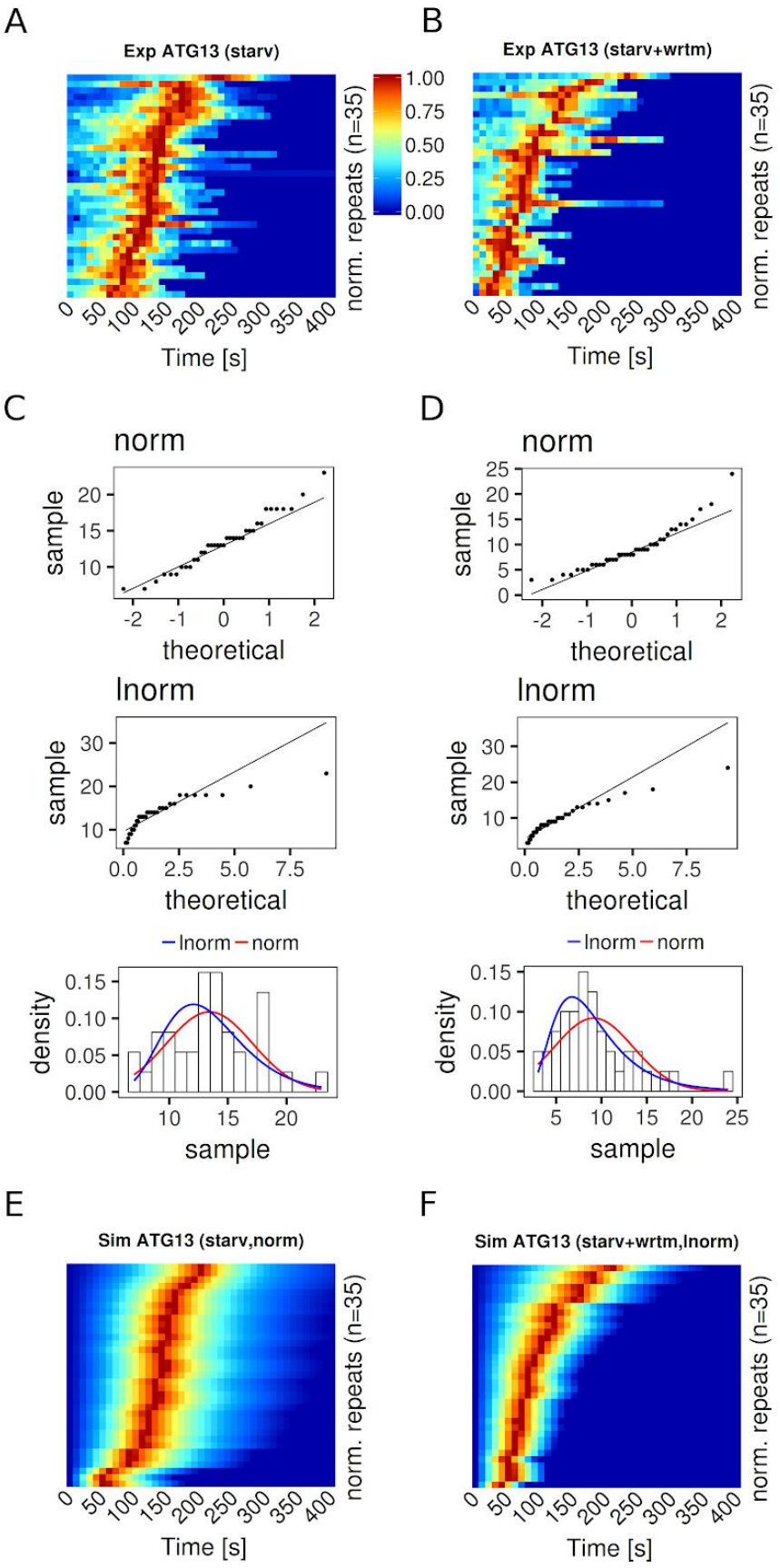

Figure 2. PI3P inhibition upon Wortmannin shifts ATG13 peak time distribution from normal to log-normal.

A. Experimental kymographs of ATG13 upon starvation. For each group n=35 experimental repeats were selected and the signal intensity of each repeat was normalised within [0,1] and indicated with the colours [blue, red]. Repeats were sorted by decreasing peak time.
B. Equivalent to panel A but for ATG13 upon starvation plus wortmannin.
C. Normality and log-normality analysis of experimental peak times for ATG13 time courses upon starvation confirmed that the peak times were normally distributed.
D. Equivalent to panel C but for ATG13 upon starvation + wortmannin. Peak times for ATG13 were log-normally distributed.
E. Simulated kymographs of ATG13 upon starvation. ATG13 peak time (parameter *t*) was sampled from a normal distribution. A total of n=35 simulated repeats were computed and the signal intensity of each repeat was normalised within [0,1] and indicated with the colours [blue, red]. Repeats were sorted by decreasing peak time.
F. Equivalent to panel E, but for ATG13 upon starvation + wortmannin. ATG13 peak time (parameter *t*) was sampled from a log-normal distribution using meanlog and sdlog.

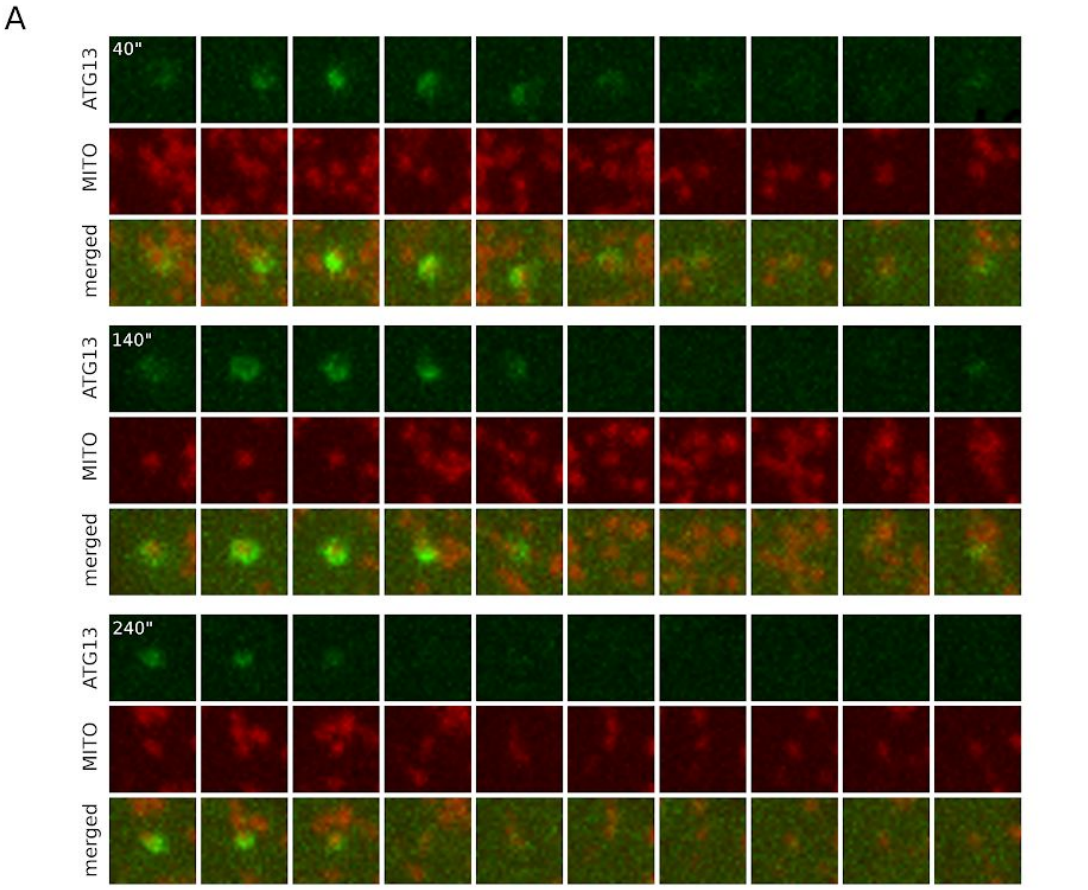

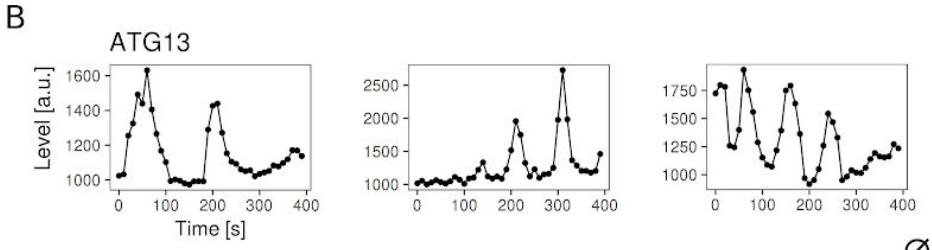

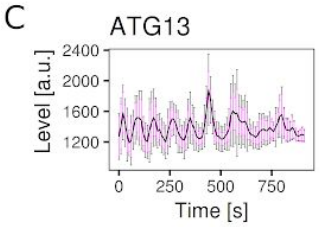

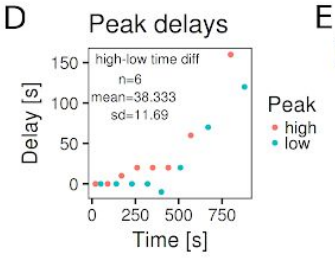

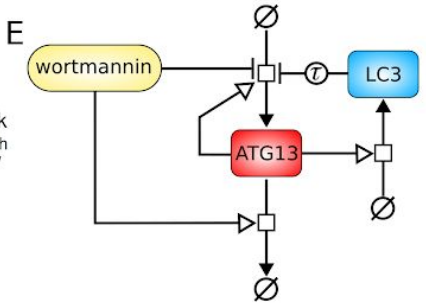

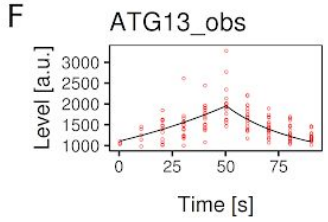

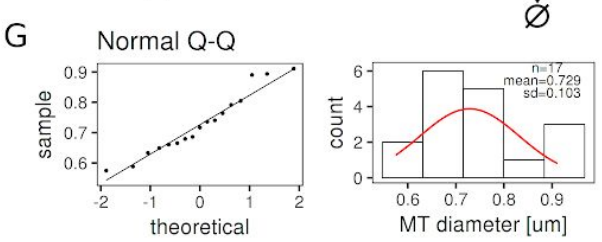

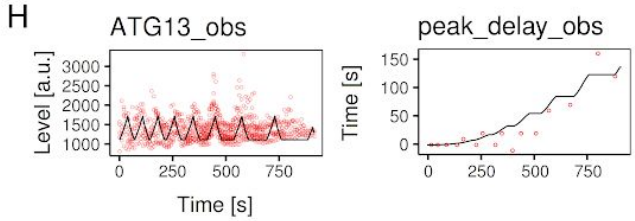

Figure 3. A mathematical model for mitophagy.

A. Representative time course images of mitophagy events. ATG13 (green) aggregates on the targeted mitochondrion (red) in multiple events. Each row depicts a phase of aggregation-detachment.

B. Three representative regularised quantified time courses up to 400s. The last panel corresponds to the images in panel A.

C. ATG13 mean time course (black line) after data synchronisation, filtering, and regularisation. The mean is shown with the confidence interval of the mean at 95% confidence level (magenta bars) and 1 standard deviation (black bars).

D. The delays of the upper and lower aggregation peaks, indicating how these increased over time exponentially. Mean and standard deviation of the time differences between upper and lower peaks are reported as annotation. These statistics define the model parameter *t*.

E. Model diagram for mitophagy events. This model extends the diagram in **Figure 1B** by including LC3 and the events for regulating the delays between aggregations. The concentration of LC3 was calculated before the event starting ATG13 accumulation was triggered. Therefore LC3 inhibits ATG13 accumulation after a delay (Tau).

F. Model fitting for ATG13 kinetic rate constants using the 1st aggregation data set. The experimental data and model simulation are represented with red circles and black line, respectively.

G. MT diameter density and QQ plot against a normal distribution. 17 mitochondrial diameters were measured and analysed. The reported mitochondria diameter mean and standard deviation define the model parameter *MT_diam*.

H. Model fitting for ATG13 and the delay between aggregations using the data sets in panel E. The parameters *t* and *MT_diam* were fixed to their mean value during this stage of parameter estimation.

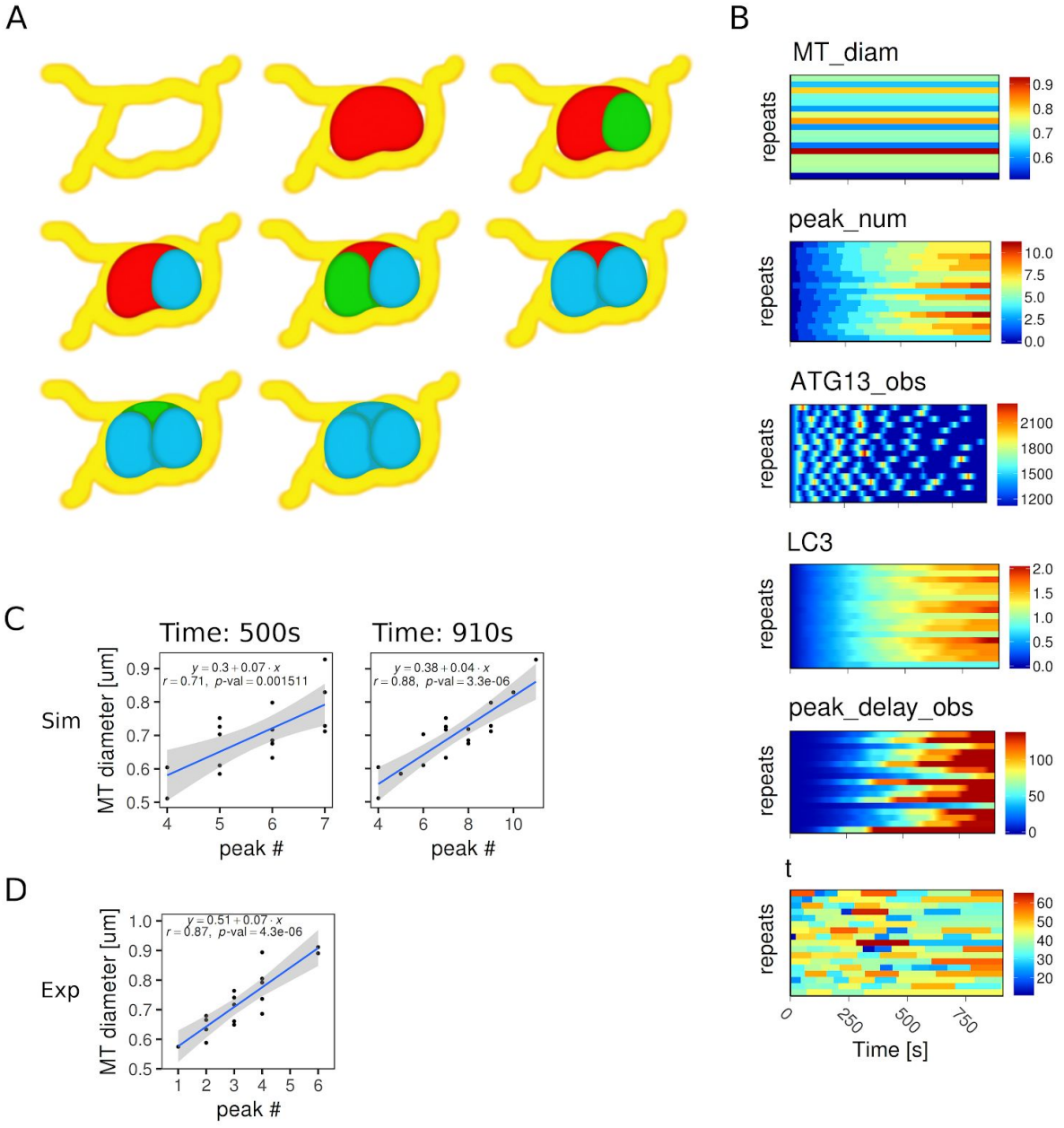

Figure 4. ATG13 aggregations number depends on the mitochondrial size.

A. Proposed model for the multiple events of selective autophagy of a mitochondrion on the ER (yellow). The targeted mitochondrion (red) translocates to a structurally compatible platform of the ER. Through repeated events ATG13 (green), followed by

LC3 (blue) covers a distinct partial surface of the mitochondrion, until the latter is completely engulfed.

B. A population of 17 mitophagy events was simulated by sampling the mitochondrial diameter (model parameter: *MT_diam*) and ATG13 accumulation time (model parameter: *t*) from their normal distributions, respectively. The single time course repeats are plotted by row on each plot. The signal intensity is depicted with the coloured scale. ATG13 signalling is shown to oscillate in each repeat and these aggregations gradually becomes unsynchronised due to the accumulation of delay between events.

C. The model predicted a linear positive correlation between the mitochondrial diameters (Panel B, MT_diam) and the number of ATG13 aggregations (Panel B, peak_num at 500s and 910s). The fitting line is indicated in blue, whereas its confidence interval in grey.

D. The previous prediction was confirmed experimentally, reporting very similar correlation and fitting line coefficients to the model prediction.

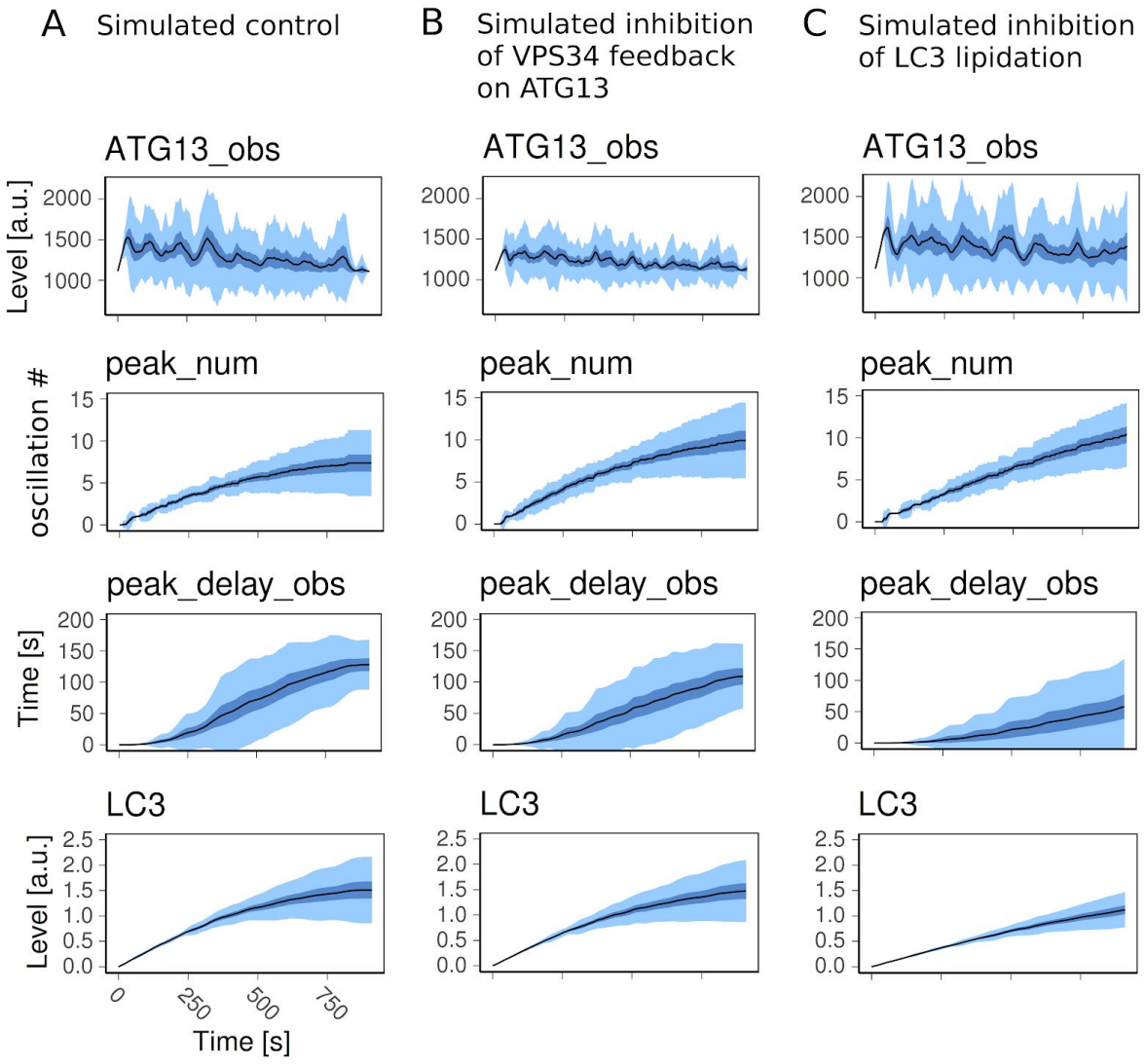

Figure 5. Effect of ATG13 or LC3 inhibition on ATG13 aggregations.

A. Summarised time courses for the readouts shown in Figure 4B. These simulated data indicate the control. The black line indicates the mean, the grey area indicates the confidence interval of the mean at each time point, and the blue area indicates 1 standard deviation of 17 repeats.

B. Simulated inhibition of VPS34 feedback on ATG13 by simulated wortmannin. The model parameter *t* was sampled from a log-normal distribution as revealed from data analysis of the non-selective autophagy model. The parameter *MT_diam* was sampled from its normal distributions. The time courses for the main model readouts

are summarised. This simulated treatment predicted an increased number of ATG13 aggregations of reduced intensity.

C. Simulated inhibition of LC3 lipidation by doubling the model parameter *EC50ATG13*. The model parameters *t* and *MT_diam* were sampled from their normal distribution. This simulated treatment predicted a time shift of the delay between aggregations causing more synchronised ATG13 accumulations in the first part of the time course. In order to cover the whole mitochondria surface, LC3 inhibition leaded to an increase in the number of ATG13 aggregations of 17 repeats.

Supplementary Information for Dynamic modelling suggests differential mechanisms for initiation of non-selective autophagy and mitophagy

Piero Dalle Pezze, Eleftherios Karanasios, Varvara Kandia, Simon Walker, Nicholas Ktistakis, and Nicolas Le Novère

The Babraham Institute, Babraham Research Campus, Cambridge, CB22 3AT, UK

Table of Contents

A) ATG13 ODE for Models 1 and 4

$$\frac{d([ATG13]\cdot V_{ER})}{dt} = +V_{ER}\cdot\left(\frac{kprodATG13\cdot[ATG13]^{m}}{1+\left(\frac{wrtm}{kwrtm}\right)^{n}}\right) - V_{ER}\cdot(kremATG13\cdot[ATG13]^{1+m})$$

B) ATG13 ODE for Models 2 and 5

$$\frac{d([ATG13]\cdot V_{ER})}{dt} = +V_{ER}\cdot(kprodATG13\cdot[ATG13]^{m}) - V_{ER}\cdot\left(kremATG13\cdot[ATG13]^{1+m}\cdot\left(1+\left(\frac{wrtm}{kwrtm}\right)^{n}\right)\right)$$

C) ATG13 ODE for Models 3 and 6

$$\frac{d([ATG13]\cdot V_{ER})}{dt} = +V_{ER}\cdot\left(\frac{kprodATG13\cdot[ATG13]^{m}}{1+\left(\frac{wrtm}{kwrtm}\right)^{n}}\right) - V_{ER}\cdot\left(kremATG13\cdot[ATG13]^{1+m}\cdot\left(1+\left(\frac{wrtm}{kwrtm}\right)^{n}\right)\right)$$

D) Assignments for Models 1-6

$$ATG13\_obs = ATG13\_sf\cdot[ATG13]$$

$$wrtm = \begin{cases} wrtm\_flag = 0, & \frac{0}{wrtm\_sf} \\ else, & \frac{wrtm\_si}{wrtm\_sf} \end{cases}$$

$$wrtm\_scaled = wrtm\_sf\cdot wrtm$$

Supplementary Table S1. ODE table for non-selective autophagy models 1-6.

The ODE regulating ATG13 dynamics differs among model 1-6, depending on the positive interaction between PI3P and ATG13. As the model does not include PI3P explicitly, PI3P inhibitor wortmannin was modelled to directly inhibit ATG13. Models 1-3 and 4-6 share the same ODE, correspondingly, but models 4-6 do not include events. A)Wortmannin downregulates ATG13 accumulation. B) Wortmannin upregulates ATG13 removal. C) Wortmannin downregulates ATG13 accumulation and upregulates ATG13 removal. D) the assignment variables shared in all the model variants. *ATG13_obs* is the only model observable which is associated to the experimental data during parameter estimation. *Wrtm_flag* is a boolean variable indicating the presence or absence of wortmannin in the model. When set to 1, *wrtm* negatively affects ATG13 dynamics.

A) ATG13_accumulation (fire at start)

Trigger expression

Time < t

Target

kprodATG13 ← kprodATG13.InitialValue

kremATG13 ← 0

B) ATG13_removal

Trigger expression

kprodATG13 > 0 and kremATG13 = 0

Delay (calculation and assignment)

t

Target

kprodATG13 ← 0

kremATG13 ← kremATG13.InitialValue

C) ATG13_basal

Trigger expression

kprodATG13 = 0 and kremATG13 > 0 and [ATG13] < 1

Target

kprodATG13 ← 0

kremATG13 ← 0

Supplementary Table S2. Events table for non-selective autophagy model 1-3.

Models 1-3 include 3 events which regulate the switch between ATG13 accumulation and removal. A) The estimated parameter *t* represents the time point when the switch between the two reaction happens. While *Time* is lesser than *t*, ATG13 can only accumulate. B) ATG13 removal is regulated by a delay event which is triggered after *t* seconds of ATG13 accumulation. C) Once ATG13 is below a certain level (after ATG13 removal), ATG13 returns to its basal level.

Model	Parameter	Value	LeftCI66	RightCI66	LeftCI95	RightCI95	LeftCI99	RightCI99
m1	kprodATG13	0.00932224	0.0062057	0.0193744	0.00534413	0.0204578	0.00485426	0.0215034
	kremATG13	0.00364467	0.00130477	0.0131757	0.000925171	0.0200528	0.000669717	0.0263238
	kwrtm	1.36189	0.633578	2.53802	0.448353	2.95053	0.404588	3.58819
	m	0.872221	-Inf	1.37514	-Inf	1.60431	-Inf	1.7034
	t	225.965	210.457	241.2	203.19	250.158	193.289	257.067
m2	kprodATG13	0.00815308	0.00408281	0.0161227	-Inf	Inf	-Inf	Inf
	kremATG13	0.00261136	1.92E-05	0.0131946	-Inf	0.0223888	-Inf	0.0381103
	kwrtm	0.603469	0.0266956	Inf	-Inf	Inf	-Inf	Inf
	m	0.79801	-Inf	2.40739	-Inf	Inf	-Inf	Inf
	t	224.952	150.113	246.585	-Inf	259.689	-Inf	269.753
m3	kprodATG13	0.00822279	0.00528378	0.0168838	0.00523032	0.0192829	0.00484189	0.0202791
	kremATG13	0.00284586	0.000990108	0.00984171	0.000703241	0.0182583	0.000577289	0.0254441
	kwrtm	1.73235	0.860786	2.94654	0.638663	3.97607	0.475282	4.55836
	m	1.01365	0.164715	1.60609	-Inf	1.64505	-Inf	1.7628
	t	225.454	211.687	240.292	199.711	249.436	195.022	257.942
m4	kprodATG13	0.0126804	0.00493445	0.212659	-Inf	Inf	-Inf	Inf
	kremATG13	0.00311011	0.00126824	0.0555853	-Inf	2966.03	-Inf	3104.35
	kwrtm	1.8235	1.04228	2.86918	0.836667	3.57971	0.701413	6.65874
	m	1.85612	-Inf	4.39006	-Inf	Inf	-Inf	Inf
m5	kprodATG13	0.00930788	0.00473933	0.133868	-Inf	Inf	-Inf	Inf
	kremATG13	0.00225599	0.00122831	0.0347083	-Inf	2902.18	-Inf	3094.07
	kwrtm	1.47676	0.910535	2.37755	0.75612	3.50593	0.622059	5.9251
	m	2.2431	-Inf	4.23665	-Inf	Inf	-Inf	Inf
m6	kprodATG13	0.0106184	-Inf	0.150482	-Inf	Inf	-Inf	Inf
	kremATG13	0.00258789	-Inf	0.039112	-Inf	2870.2	-Inf	3002.41
	kwrtm	3.71053	2.45462	6.07959	1.9224	8.95748	1.61016	11.6276
	m	2.08336	-Inf	5.17864	-Inf	Inf	-Inf	Inf

Supplementary Table S3. Table of estimated parameters for the non-selective autophagy models 1-6.

For each model variant, the estimated parameter values and its confidence intervals at confidence levels of 66%, 95%, and 99% are reported. The parameter *m* indicate the degree of ATG13 protein coperativitiness during ATG13 accumulation and removal. The kinetic rate constants *kprodATG13* and *kremATG13* are the parameters regulating the mass action reactions for ATG13 accumulation and removal. The parameter *kwrtm* is the kinetic rate constant for wortmannin. The parameter *t* is the time point when the switch between ATG13 accumulation and removal occurs. Model 3 was the only one whose parameters were identifiable within a confidence level of 66%.

Other Parameters	Value
wrtm_flag	0 or 1
ATG13_sf	525
ATG13_ini	525
n	1
wrtm_ini	1500
wrtm_sf	1500

Supplementary Table S4. Additional parameters for the non-selective autophagy models 1-6.

These remaining parameters were not estimated. *Wrtm_flag* is a boolean flag indicating the presence or absence of wortmannin in the model. *ATG13_sf* and *ATG13_ini* are the scaling factor and initial value for ATG13. Their value was set to ATG13 basal level within the data. The parameter *n* indicate the degree of coperativiness for wortmannin. The value of 1 indicate no coperativiness. Finally, *wrtm_ini* and *wrtm_sf* are the scaling factor and initial value for wortmannin. These are currently fixed to a value approximating the average of ATG13 peak intensity upon wortmannin. These value do not affect the model.

Model	AIC
m1	5.69E+08
m2	8.92E+08
m3	5.85E+08
m4	8.95E+08
m5	8.88E+08
m6	8.90E+08

Supplementary Table S5. AIC scores for models 1-6.

Models 1 and 3 reported the best fitting quality and were the only one fitting the data correctly. Model 3 was chosen as it offered a more general biological mechanism of wortmannin interaction with ATG13.

Peak times	starvation	starvation+wortmannin
mean	134.3243243	91.5
sd	36.70759387	43.41511021
skewness	0.3123986084	1.193015561
kurtosis (excess)	-0.2506456494	1.715914161
mean *	4.862389097	4.413028409
sd *	0.2839778206	0.4647363216
skewness *	-0.3430226437	-0.1160637561
kurtosis (excess) *	-0.4434826787	-0.1979578255
meanlog (for lnorm distrib) **	4.864245879	4.414814168
sdlog (for lnorm distrib) **	0.268370368	0.4506102617
* calculated using log(data).		
** parameters used when sampling from a log-normal distribution.		

Supplementary Table S6. Descriptive statistics for non-selective autophagy data set.

Descriptive statistics were generated for the time courses. Statistics for the time courses peak times were collected. Skewness and excess kurtosis for the starvation+wortmannin data set indicate how this distribution is not close to a normal distribution compared to the starvation data set, where the values are closer to 0. The same statistics were calculated using the log of the two data sets. Whilst for starvation data set this result indicates a marginal drift from a normal distribution, for the starvation+wortmannin data set the skewness and kurtosis report a closer overlap with a normal distribution, supporting the fact that the original data set was log-normally distributed. We also computed the meanlog and sdlog, which are the parameters for a log-normal distribution from the corresponding normal distribution. The parameters for peak times and lnorm peak times are highlighted and were used for sampling the peak times from a normal or log-normal distribution, respectively, for the simulations reported in Figure 2E-F. Meanlog and sdlog were computed as follows:

meanlog <- function(mu, v) { log((mu^2)/sqrt(v+mu^2)) }

sdlog <- function(mu, v) { sqrt(log(v/(mu^2)+1)) }

Where *mu* and *v* are the usual mean and variance. Therefore, the log-normal distribution was generated as:

lognormal <- e^normal(meanlog, sdlog)

$$\frac{d([ATG13]\cdot V_{ER})}{dt} = +V_{ER}\cdot\left(\frac{kprodATG13\cdot[ATG13]^{m}}{1+\left(\frac{wrtm}{kwrtm}\right)^{n}}\right) -V_{ER}\cdot\left(kremATG13\cdot[ATG13]^{1+m}\cdot\left(1+\left(\frac{wrtm}{kwrtm}\right)^{n}\right)\right)$$

$$\frac{d([LC3]\cdot V_{ER})}{dt} = +V_{ER}\cdot\left(kprodLC3\cdot\frac{[ATG13]}{EC50ATG13+[ATG13]}\right)$$

$$ATG13\_obs = ATG13\_sf\cdot[ATG13]$$

$$wrtm = \begin{cases} wrtm\_flag = 0, & \frac{0}{wrtm\_sf} \\ else, & \frac{wrtm\_si}{wrtm\_sf} \end{cases}$$

$$ATG13\_sf = ATG13\_min$$

$$wrtm\_scaled = wrtm\_sf\cdot wrtm$$

$$EC50ATG13 = \frac{ATG13\_max - ATG13\_min}{2}$$

$$cf = \frac{[LC3]}{MT\_surf}$$

$$peak\_delay\_obs = kpeak\cdot cf^{p}$$

Supplementary Table S7. ODE table for mitophagy model.

This model extends the third model for non-selective autophagy with the inclusion of LC3 and the peak delay observable (variable *peak_delay_obs*). LC3 is positively regulated by ATG13 and its production is arrested by an event triggered when the simulated mitochondrion is engulfed. The peaks delay is calculated from the fraction of mitochondrion surface (parameter *MT_surf=pi*MT_diam^2*) that is covered by LC3 (parameter *cf*). In absence of LC3, *cf* is 0 and there is no delay between peaks. When the mitochondrion is completely engulfed, *cf* is 1 and the delay will be maximised (=*kpeak*). At this stage an event triggers the end for the simulation of ATG13 and LC3.

A) ATG13_accumulation (fire at start)

Trigger expression

ATG13_obs <= ATG13_min and kremATG13 = 0 and cf < 1

Delay (calculation and assignment)

peak_delay_obs

Target

kprodATG13 ← kprodATG13.InitialValue
kremATG13 ← 0
t ← normal(38.33333333,11.6904519445)
time_fire ← Time
kprodLC3 ← kprodLC3.InitialValue

B) ATG13_removal (fire at start)

Trigger expression

kprodATG13 > 0 and Time >= time_fire + t

Target

kprodATG13 ← 0
kremATG13 ← kremATG13.InitialValue
peak_num ← peak_num + 1

C) ATG13_basal (fire at start)

Trigger expression

ATG13_obs <= ATG13_min and kremATG13 > 0

Target

kprodATG13 ← 0
kremATG13 ← 0
kprodLC3 ← 0
ATG13 ← ATG13_min / ATG13_sf

D) MT_engulfed (fire at start)

Trigger expression

cf >= 1

Target

kprodATG13 ← 0
kremATG13 ← kremATG13.InitialValue
kprodLC3 ← 0

Supplementary Table S8. Events table for mitophagy model.

ATG13 accumulation and removal events regulate the ATG13 process. The first event is delayed depending on the stage of mitochondrion engulfment by LC3 (*peak_delay_obs*). When triggered, the parameter *t* and *time_fire* which regulate the triggering for ATG13 removal event are also updated. In the two steps of parameter estimations, the parameter *t* is fixed to 50 (parameter estimation for the 1st peak) and 38.33333333 (the mean time difference between upper and lower peaks). The last two events control the end of the simulation when the simulated mitochondrion has been engulfed (*cf* >= 1).

Step	Round	Parameter	Value	LeftCI66	RightCI66	LeftCI95	RightCI95	LeftCI99	RightCI99
1st peak	1	kprodATG13	0.0113491	0.0105062	0.0122197	0.00989427	0.0127426	0.00950567	0.0130256
		kremATG13	0.0113493	0.0105583	0.0125588	0.0099646	0.0139121	0.0095942	0.0148284
n peaks	1	kprodLC3	0.779693	0.315287	0.867601	0.251537	0.999483	0.188636	1.02112
		p	2.78977	2.26954	3.26076	1.91662	3.5024	1.63998	9.25167
		kpeak	135.796	101.526	Inf	72.9858	Inf	66.9902	Inf
	2	kpeak	136.137	127.481	143.216	119.836	151.299	115.046	156.433

Supplementary Table S9. Tables of estimated parameters for the mitophagy model.

Parameter estimation for the mitophagy model was performed in two steps. In the first step the kinetic rate constants for ATG13 accumulation and removal reactions were estimated using only the first peak time course data. These parameters were identifiable. In the second step the kinetic rate constant regulating LC3 production and the two parameters regulating the peak delay observable (*p* and *kpeak*) were estimated. *kpeak* was practically non identifiable at this stage because partially related to *kprodLC3*. The identifiable parameters *kprodLC3* and *p* were fixed, whilst *kpeak* was re-estimated (round 2). This allowed us to calculate confidence intervals for all the model parameters.

A Mitophagy (first step of parameter estimation)

Other Parameters	Value
wrtm_flag	0
ATG13_min	1111.71
t	50
ATG13_max	1779.31
time_fire	0
peak_num	0
MT_surf	Pi * MT_diam^2
MT_diam	0.7285371148

B Mitophagy (second step of parameter estimation)

Other Parameters	Value
t	38.33333333

C Mitophagy (simulation)

Other Parameters	Value
t (at each evt)	Normal(38.33333333,11.6904519445)
MT_diam	Normal(0.7285371148,0.103021783)

Supplementary Table S10. Additional parameters for the mitophagy model.

The mitophagy model includes other parameters which were not estimated but determined by experimental data analysis. A) Values for the additional parameters during the first step of parameter estimation. The parameter *t* is set to 50 as this is the time when the time courses for the first peak were synchronised. It corresponds to the time when ATG13 accumulation reaction is interrupted and ATG13 is activated. The parameter *MT_diam* is set to the mean of the mitochondria diameters distribution. B) For the second step, the parameter *t* is updated to the mean value of its distribution. C) After parameter estimation, the parameters *t* and *MT_diam* are sampled from their normal distributions. The mitochondrial diameter is sampled at the beginning of each simulation, whereas the parameter t is sampled at each ATG13 aggregation.

name	value
mean	38.33333333
sd	11.69045194
skewness	0.8808986197
kurtosis (excess)	-0.90427325
meanlog (lnorm)	3.601854141
sdlog (lnorm)	0.298213678

Supplementary Table S11. Descriptive statistics for the peak times across peaks.

Descriptive statistics were generated for the time differences between the upper and lower peaks of each peak using the mean ATG13 time course. Despite the peak times for a single peak tend to be normally distributed, the peak times across peaks tend to be less than normal as the skewness and excess kurtosis indicate. We also computed the meanlog and sdlog for the log-normal distribution. The log-normal distribution was computed as described in **Supplementary Table S6**.

Step	Round	AIC
1st peak	1	1.20E+07
n peaks	1	1.03E+08
	2	1.03E+08

Supplementary Table S12. AIC score for the mitophagy model.

AIC scores for each round of parameter estimation were calculated. There was no improvement in model fitting in the second round of the second step of parameter estimation.

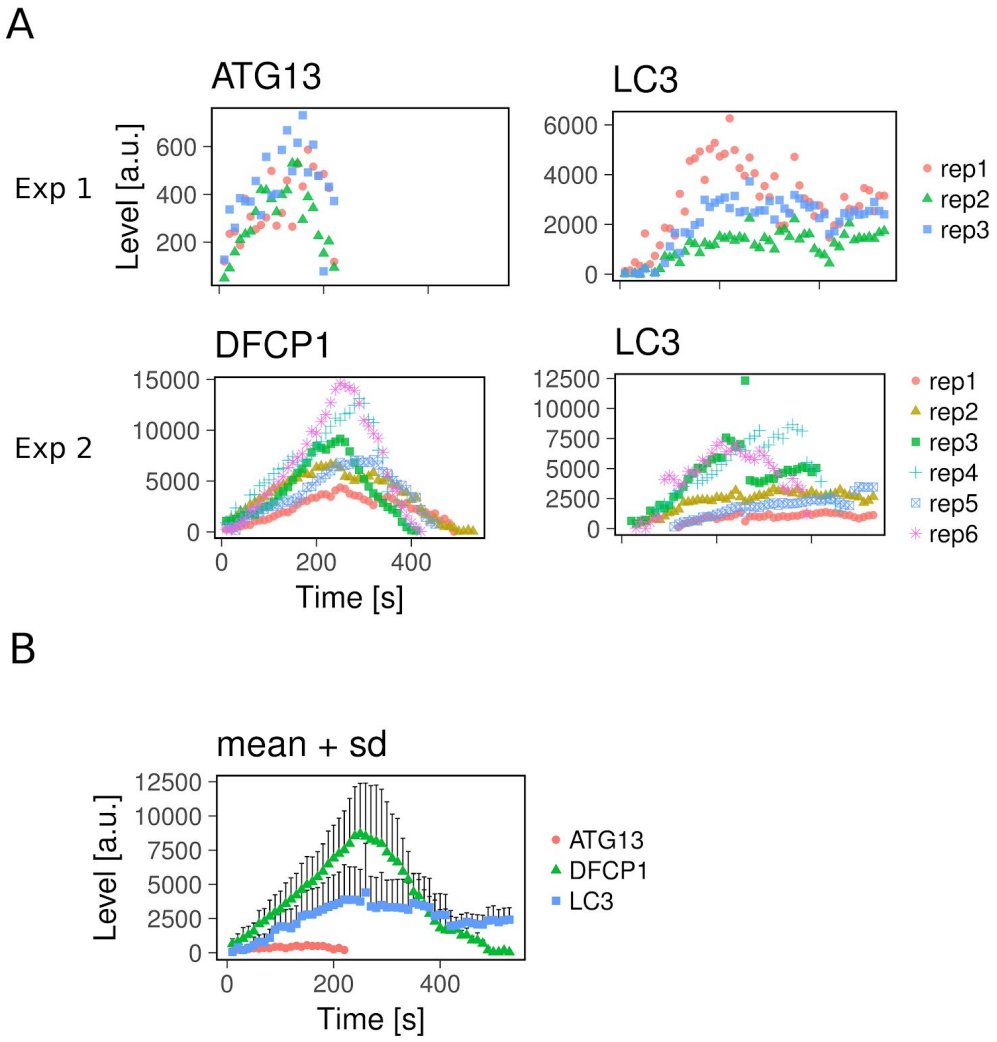

Supplementary Figure S1. Preliminary data for ATG13, DFCP1, and LC3 using wide field microscopy.

Quantified experimental time courses from wide field images. **A**. GFP-ATG13 and CFP-LC3 or GFP-DFCP1 and CFP-LC3 were used in two experiments. ATG13 followed by DFCP1 initiate the autophagosome formation. Once mature, the autophagosome detaches from the membrane as shown in the 3rd and 6th repeats for Exp2 for LC3. **B**. Mean plus 1 standard deviation for ATG13, DFCP1, and LC3 using the data in panel A.

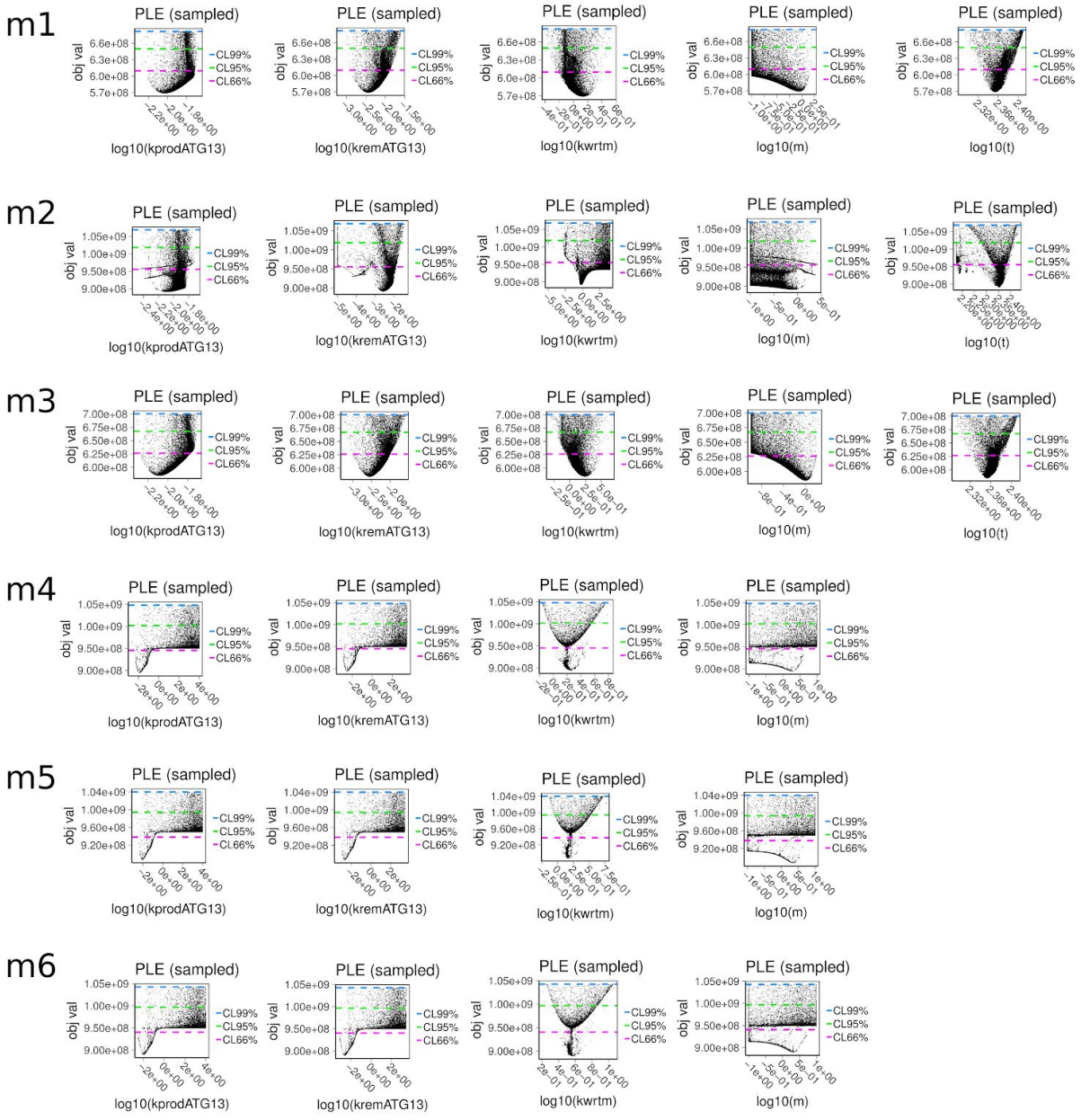

Supplementary Figure S2. PLE for the parameters of the non-selective autophagy models.

The PLE plots are represented for each estimated parameters (rows) for the six model variants (columns). For each plot, the x axis reports the parameter values in log10 space, whereas the y axis reports the model objective value. The confidence levels at 66%, 95%, and 99% are reported as coloured horizontal dashed lines. Models 1 and 3 were the only ones to fit the data and model 3 was the only one were each parameter was identifiable within a confidence level of 66%. Model 4-6 did not fit the data and their parameters resulted largely non-identifiable.

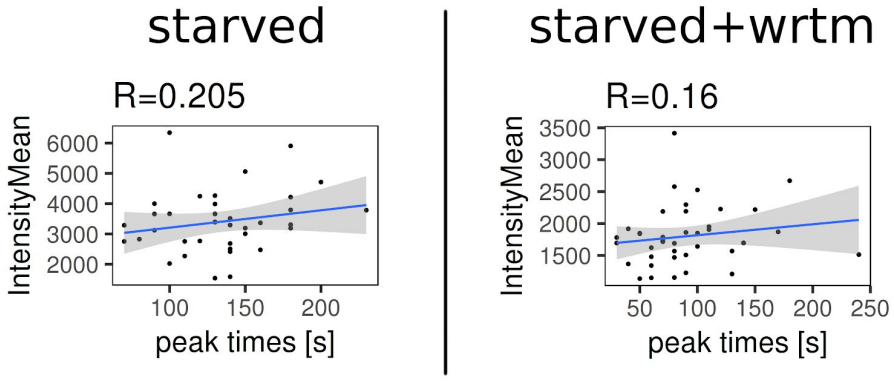

Supplementary Figure S3. Peak times did not correlate with signal intensities for the non-selective autophagy data.

No significant correlation was found between peak times and corresponding signal intensities for the starvation and starvation+wortmannin data sets in the non-selective autophagy.

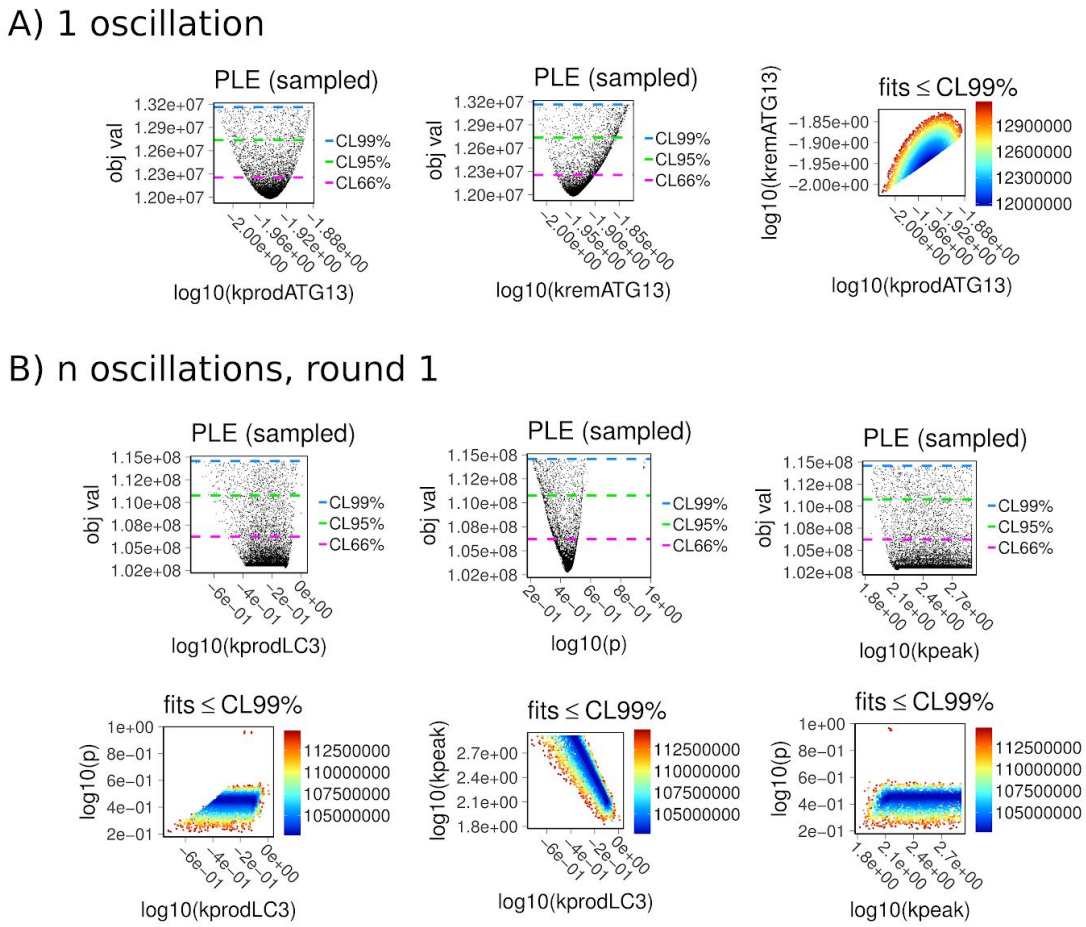

Supplementary Figure S4. PLE for the parameters of the mitophagy model.

A) Parameter estimation and identifiability using the first peak data set. ATG13 kinetic rate constants were identifiable within a confidence level of 99% and did not correlate with each other.

B) First round of parameter estimation and identifiability using the complete time course data set. In the first round of parameter estimation, the parameters *p* and *kprodLC3* were identifiable although *kprodLC3* minima lay on a plateau. The parameter *kpeak* was practically non-identifiable (see infinite upper bound).

C) After fixing the parameters *p* and *kprodLC3*, the parameter *kpeak* was re-estimated and found identifiable.

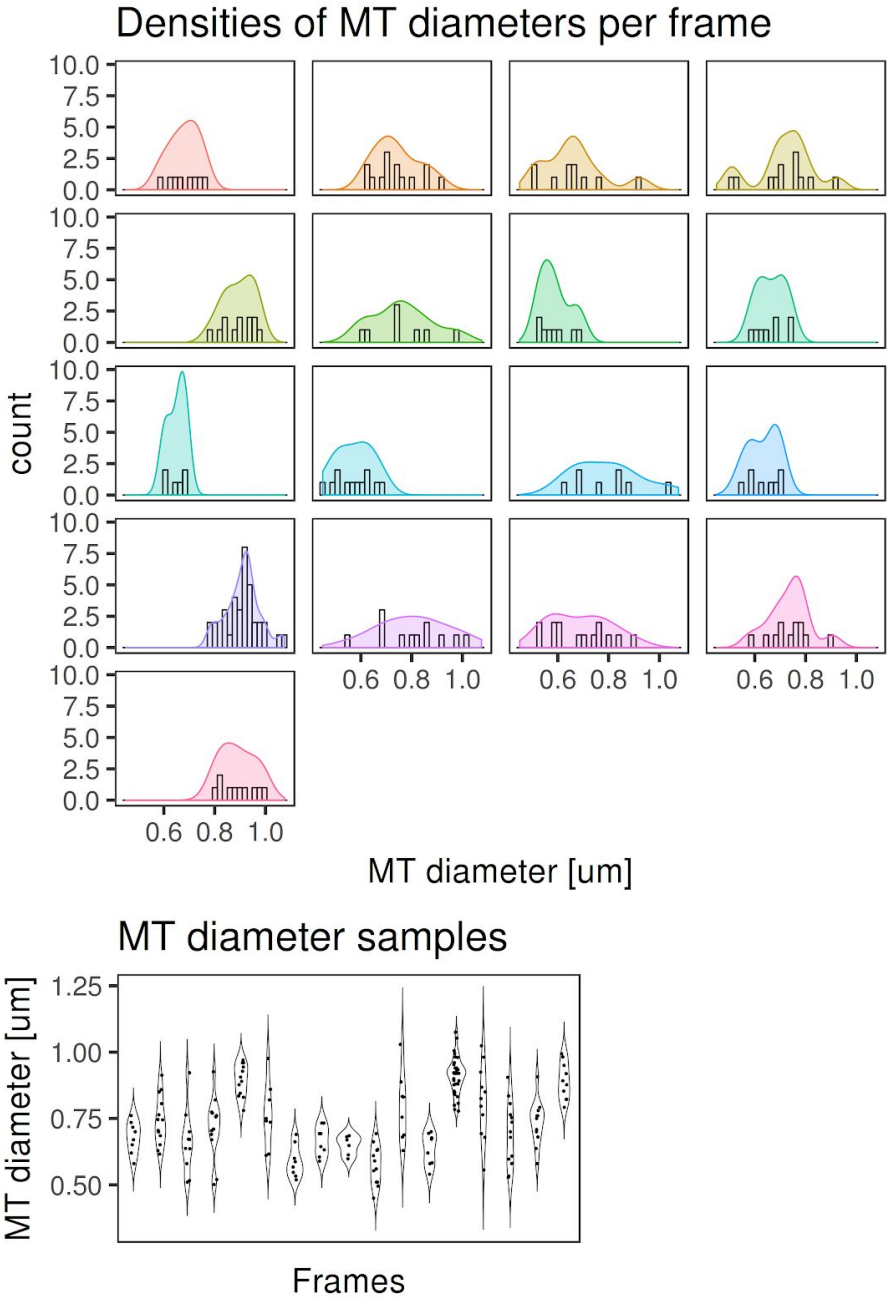

Supplementary Figure S5. Mitochondrial diameter measurements for each frame.

The diameter of the mitochondria engulfed by ATG13 were measured for each of the 17 time courses. The mean diameter for each frame was then computed.

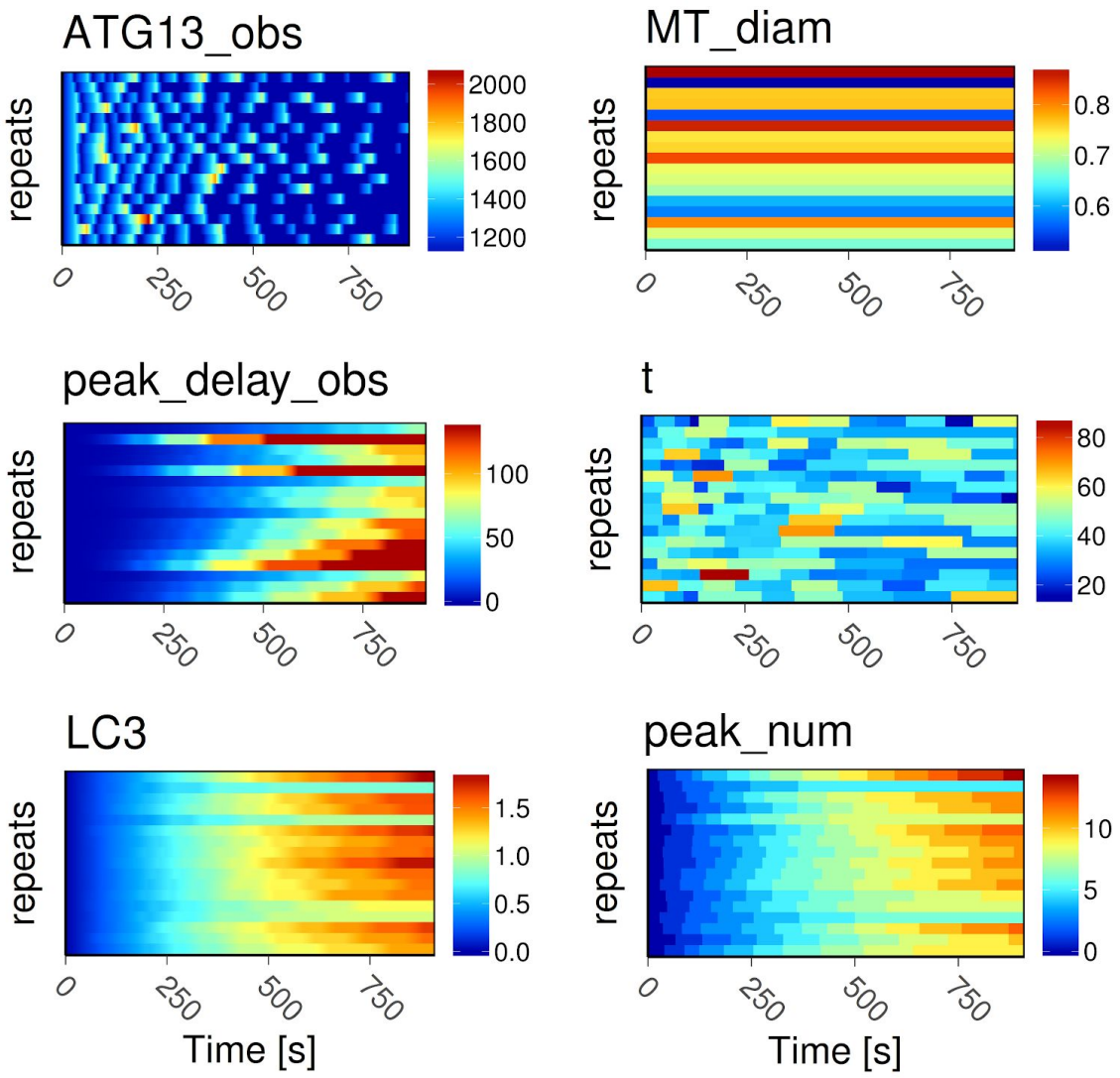

Supplementary Figure S6. Single repeats for Figure 5B (inhibition of VPS34 feedback on ATG13 by simulated wortmannin).

The time courses for the 17 repeats are plotted by row for each plot. ATG13 time courses tended to retard their desynchronisation, whereas the number of peaks increased.

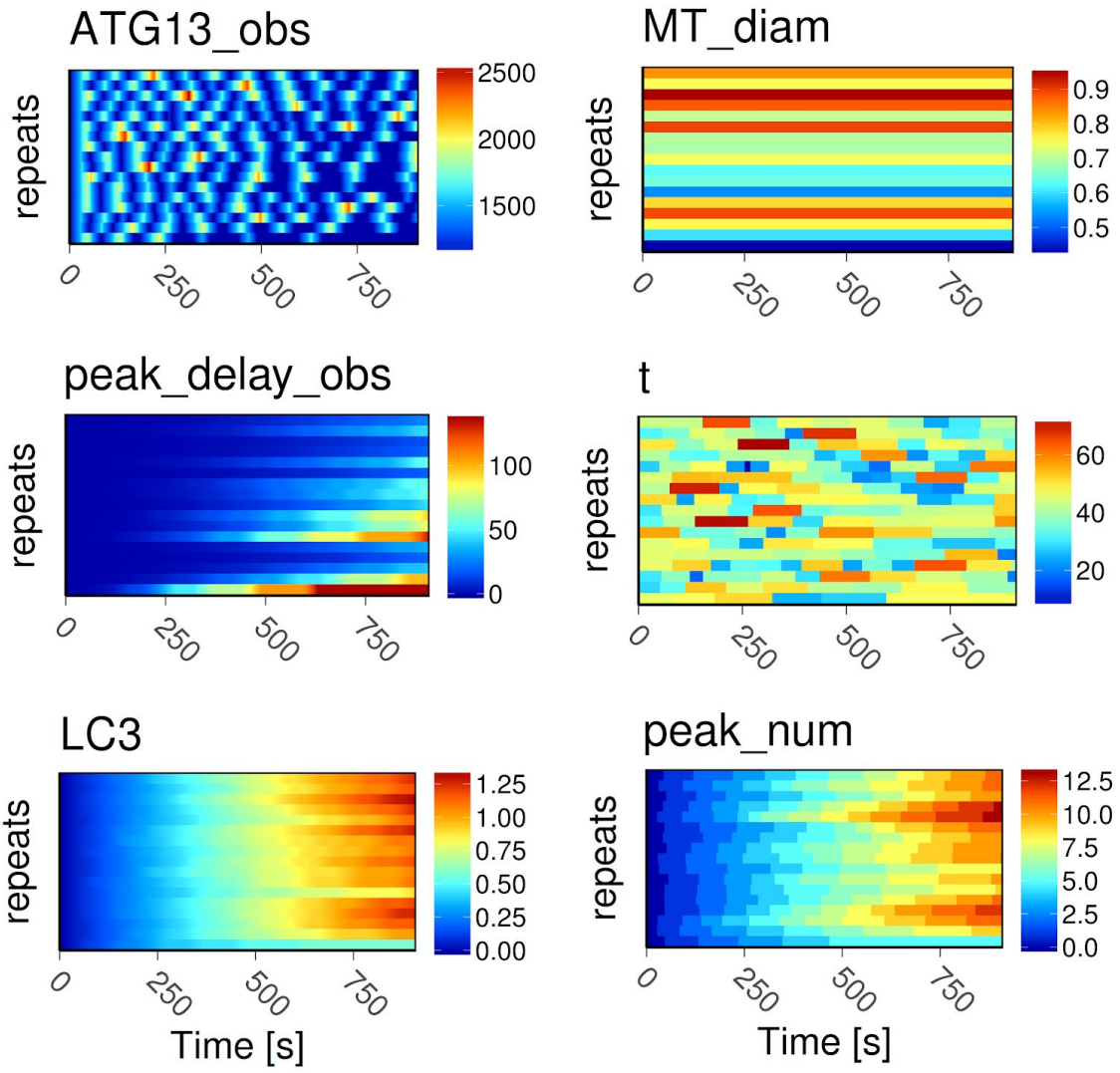

Supplementary Figure S7. Single repeats for Figure 5C (inhibition of LC3 lipidation).

The time courses for the 17 repeats are plotted by row for each plot. ATG13 time courses remained largely synchronised for the first part of the time course due to the low LC3 levels, which reduced the delay between ATG13 peaks.

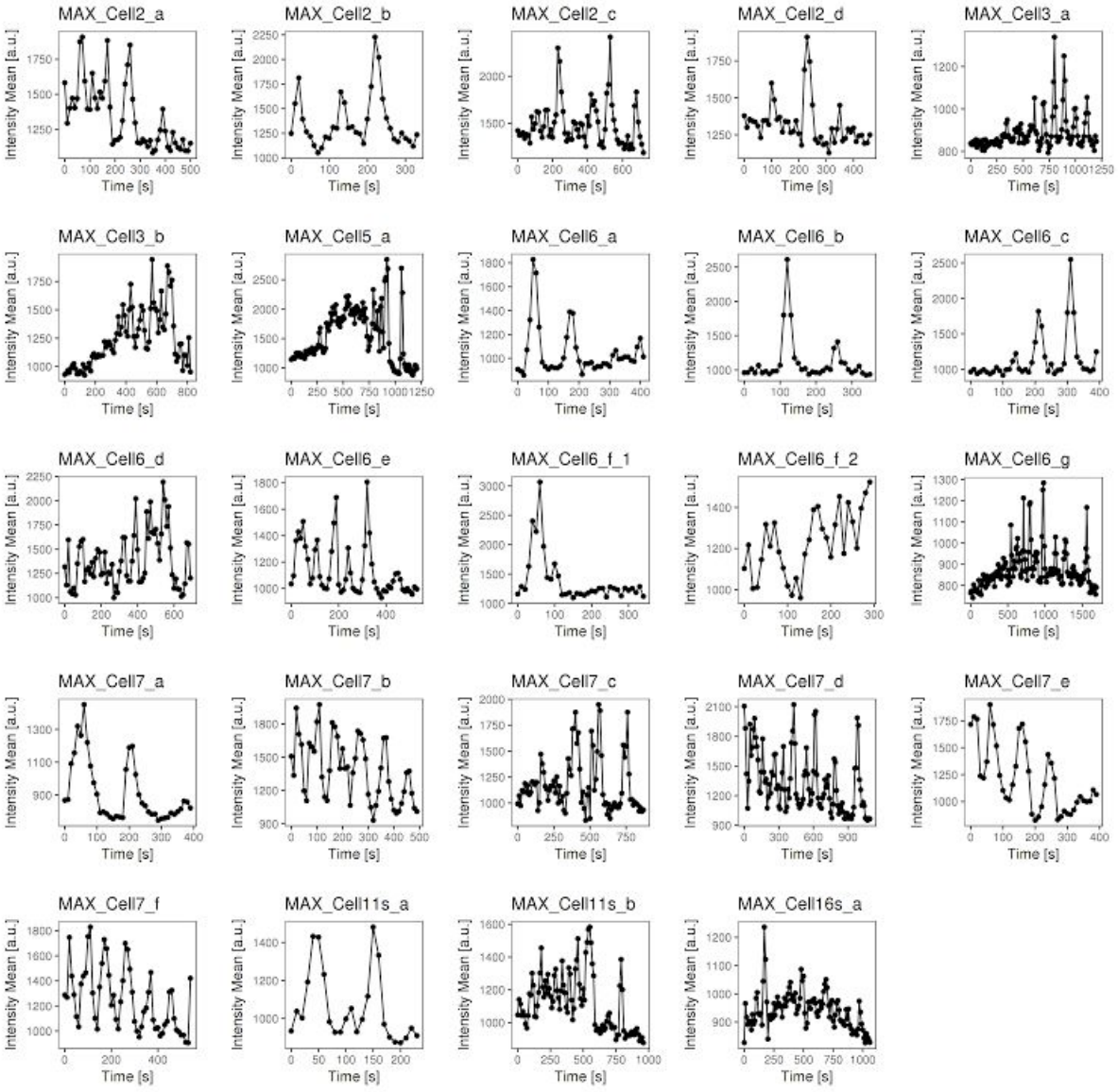

Supplementary Figure S8. Raw quantified time courses for ATG13 for the mitophagy model.

A total of 23 time courses were quantified from fluorescence large images. ATG13 accumulations/removals have similar lengths but the time between two peaks tend to increase over time. Due to this regularity, the time courses could have been synchronised.

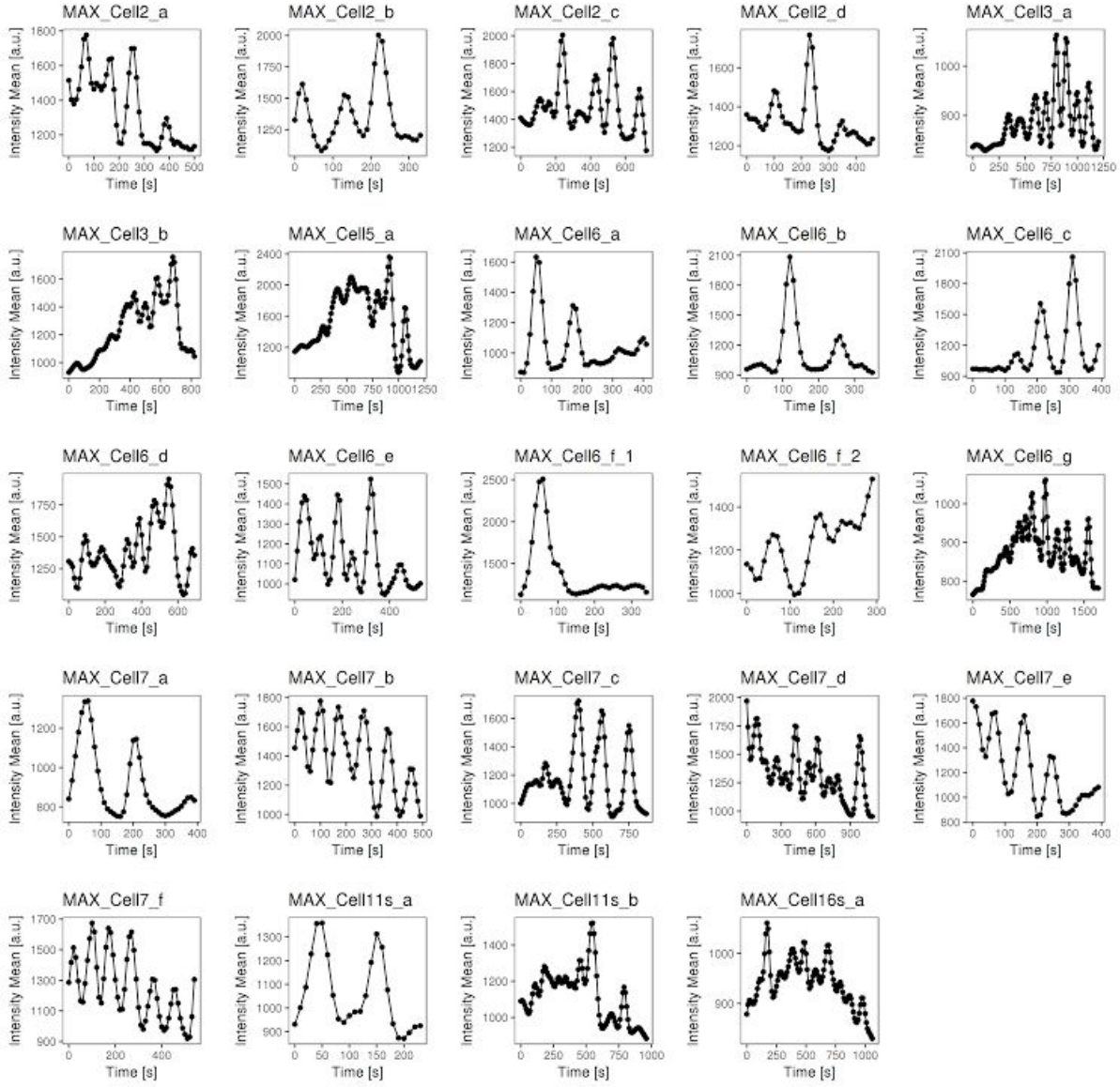

Supplementary Figure S9. Splined quantified time courses for ATG13 for the mitophagy model.

To facilitate the synchronisation, ATG13 time courses were splined in order to remove small noise in the signal and visualise the peaks more clearly. The splining of this data was performed using the R function smooth.spline() with spline parameter *spar* set to 0.4 .

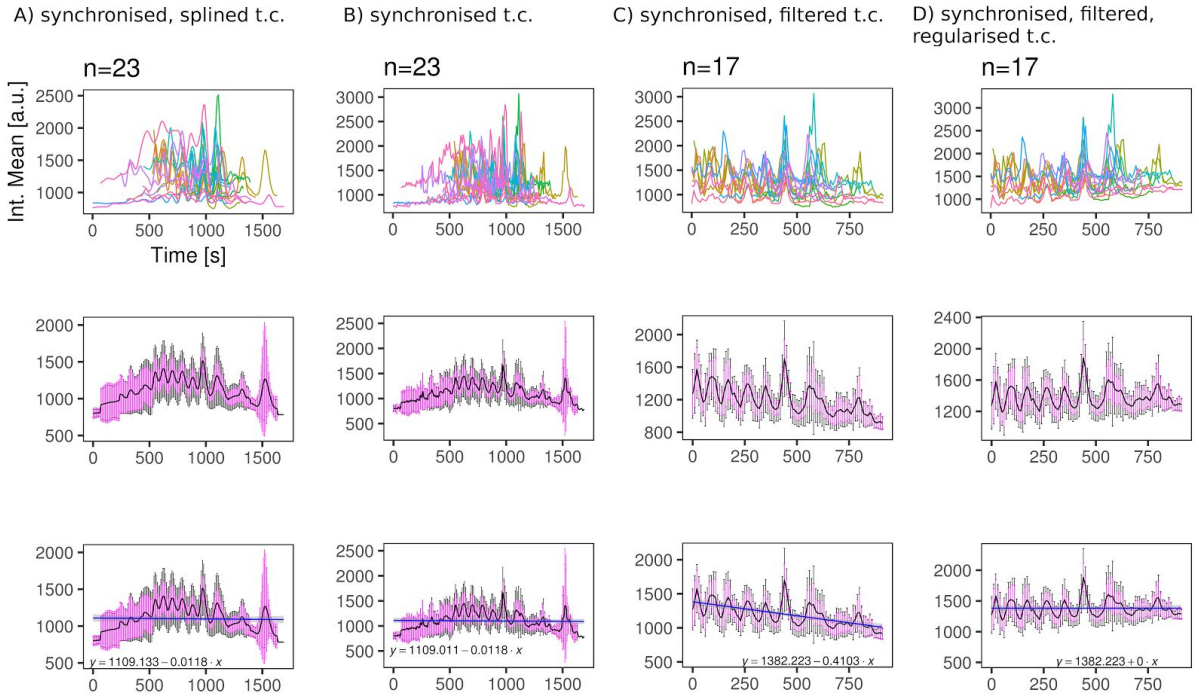

Supplementary Figure S10. Synchronisation and filtering of ATG13 time courses for the mitophagy model.

A) ATG13 splined time courses were synchronised by overlapping the delays between peaks.
B) The splined time courses were then replaced with the original ATG13 time courses.
C) Six time courses were removed because they contained too much noise in their signal. Initial and later signals were cut off in order to have at least 3 repeats for each time point.
D) The mean time course was regularised so that there was no signal decline over time. Each time course was adjusted based on this regularisation.

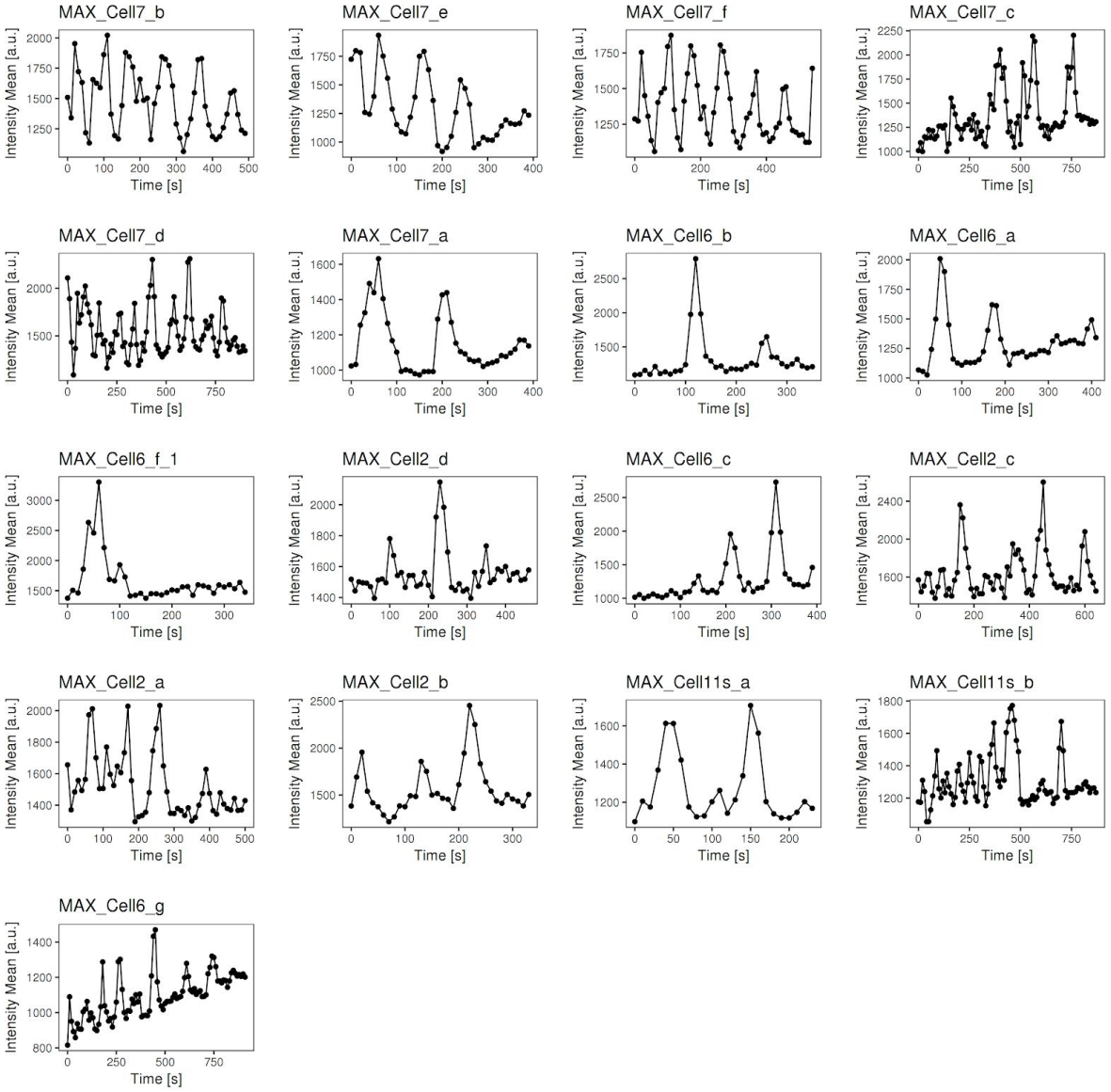

Supplementary Figure S11. ATG13 time courses for the mitophagy model after synchronisation, filtering and regularisation.

ATG13 final time courses are illustrated. The data points from this figure were used for parameter estimation of the mitophagy model.

Supplementary Model 1. Non-selective autophagy model 3.

Supplementary Model 2. Mitophagy model.